



## RESEARCH ARTICLE

10.1029/2021MS002891

# On the Vertical Structure of Oceanic Mesoscale Tracer Diffusivities

Wenda Zhang<sup>1</sup>  and Christopher L. P. Wolfe<sup>1</sup> <sup>1</sup>School of Marine and Atmospheric Sciences, Stony Brook University, Stony Brook, NY, USA

## Key Points:

- Eddies are nonlinear in the circumpolar current and transition from nonlinear to linear regimes from upper to deep ocean in the gyres
- Mixing in the nonlinear regime is well-represented by the rms eddy velocity times a depth-independent energy-containing scale
- Mixing in the linear regime follows the vertical structure of the eddy kinetic energy times a depth-independent decay time scale

## \*Correspondence to:

W. Zhang,  
wenda.zhang@stonybrook.edu

## Citation:

Zhang, W., & Wolfe, C. L. P. (2022). On the vertical structure of oceanic mesoscale tracer diffusivities. *Journal of Advances in Modeling Earth Systems*, 14, e2021MS002891. <https://doi.org/10.1029/2021MS002891>

Received 2 NOV 2021

Accepted 20 APR 2022

## Author Contributions:

**Conceptualization:** Wenda Zhang,

Christopher L. P. Wolfe

**Data curation:** Wenda Zhang,

Christopher L. P. Wolfe

**Formal analysis:** Wenda Zhang,

Christopher L. P. Wolfe

**Funding acquisition:** Christopher L. P.

Wolfe

**Investigation:** Wenda Zhang, Christopher

L. P. Wolfe

**Methodology:** Wenda Zhang,

Christopher L. P. Wolfe

**Project Administration:** Christopher L.

P. Wolfe

**Resources:** Christopher L. P. Wolfe

**Abstract** Isopycnal mixing of tracers is important for ocean dynamics and biogeochemistry. Previous studies have primarily focused on the horizontal structure of mixing, but what controls its vertical structure is still unclear. This study investigates the vertical structure of the isopycnal tracer diffusivity diagnosed by a multiple-tracer inversion method in an idealized basin circulation model. The first two eigenvalues of the symmetric part of the 3D diffusivity tensor are approximately tangent to isopycnal surfaces. The isopycnal mixing is anisotropic, with principal directions of the large and small diffusivities generally oriented along and across the mean flow direction. The cross-stream diffusivity can be reconstructed from the along-stream diffusivity after accounting for suppression of mixing by the mean flow. In the circumpolar channel and the upper ocean in the gyres, the vertical structure of the along-stream diffusivity follows that of the rms eddy velocity times a depth-independent local energy-containing scale estimated from the sea surface height. The diffusivity in the deep ocean in the gyres instead follows the profile of the eddy kinetic energy times a depth-independent mixing time scale. The transition between the two mixing regimes is attributed to the dominance of nonlinear interactions and linear waves in the upper and deep ocean, respectively, distinguished by a nonlinearity parameter. A formula is proposed that accounts for both regimes and captures the vertical variation of diffusivities better than extant theories. These results inform efforts to parameterize the vertical structure of isopycnal mixing in coarse-resolution ocean models.

**Plain Language Summary** Ocean mesoscale eddies mix momentum, heat, carbon and other tracers, which impacts the ocean environment and Earth's climate. The mixing of tracers by mesoscale eddies is mostly measured on the surface, but the observation of the mixing in the ocean interior is rare. It is unclear how eddy mixing varies with depth. We estimated the mixing by mesoscale eddies in an idealized numerical model, which simulates ocean currents and eddies in a basin like the Atlantic Ocean. Mixing decreases with depth in the same rate as the characteristic swirling velocity of eddies in the upper ocean, while it decreases faster in the deep ocean. This is because as eddies become weak in the deep ocean they behave like waves rather than closed swirls. A method accounting for this vertical variation is proposed which recovers the vertical structure of eddy mixing over full depth, once the characteristic swirling velocity is available.

## 1. Introduction

Ocean mesoscale eddies, with scales of 10–100s of kilometers, represent the majority of the kinetic energy of the ocean circulation (Ferrari & Wunsch, 2009). Stirring by mesoscale eddies plays an important role in the transport and mixing of oceanic tracers, which impacts ocean dynamics (Hallberg & Gnanadesikan, 2006; J. Marshall & Radko, 2003, 2006; Wolfe & Cessi, 2009, 2010) and biogeochemistry (Steinberg et al., 2019; McGillicuddy Jr et al., 2003; Siegenthaler, 1983; Gnanadesikan et al., 2015). The ocean components of most climate models do not resolve mesoscale eddies and their impact on tracer stirring must be parameterized. The standard parameterizations mimic two aspects of mesoscale eddy stirring: the advection of buoyancy or thickness that flattens isopycnals (“GM”, Gent & McWilliams, 1990; Gent et al., 1995, see Table 1 for a list of abbreviations used in this paper) and diffusion of tracers along isopycnals that reduces mean tracer variance (“Redi”, Redi, 1982). These two schemes can be formulated as a single rank-two diffusivity tensor with its symmetric part representing the Redi scheme and its antisymmetric part representing the GM scheme (Griffies, 1998). Model simulations are sensitive to the magnitude and distribution of the coefficients of both the GM and Redi parameterizations (J. Marshall & Radko, 2003; Gnanadesikan et al., 2015; J. Marshall et al., 2017; Jones & Abernathey, 2019), and so these coefficients must be constrained by physical insight or measurement. Many theoretical studies have focused on the GM coefficient (e.g., Visbeck et al., 1997; Cessi, 2008; D. P. Marshall & Adcroft, 2010; D. P. Marshall et al., 2012; Jansen et al., 2015), leaving the Redi coefficient less well constrained in climate models.

© 2022 The Authors. Journal of Advances in Modeling Earth Systems published by Wiley Periodicals LLC on behalf of American Geophysical Union. This is an open access article under the terms of the [Creative Commons Attribution-NonCommercial-NoDerivs License](https://creativecommons.org/licenses/by/4.0/), which permits use and distribution in any medium, provided the original work is properly cited, the use is non-commercial and no modifications or adaptations are made.

**Software:** Wenda Zhang, Christopher L. P. Wolfe

**Supervision:** Christopher L. P. Wolfe

**Validation:** Wenda Zhang, Christopher L. P. Wolfe

**Visualization:** Wenda Zhang, Christopher L. P. Wolfe

**Writing – original draft:** Wenda Zhang

**Writing – review & editing:** Wenda Zhang, Christopher L. P. Wolfe

Observational studies have estimated the horizontal distribution of the isopycnal tracer diffusivity (i.e., the Redi coefficient) using satellite (J. Marshall et al., 2006; Ferrari & Nikurashin, 2010; R. P. Abernathy & Marshall, 2013) and in situ data (Roach et al., 2018; Zhurbas et al., 2014; Zhurbas & Oh, 2003), but direct observations of the full-depth diffusivity is only available at two sites: one in the North Atlantic (Ledwell et al., 1998) and one in the Southern Ocean (Tulloch et al., 2014). Studies have inferred the vertical structure of diffusivity based on the mixing length theory (MLT, Prandtl, 1925; Cole et al., 2015; Naveira Garabato et al., 2011) and variations that account for mean flow suppression (suppressed mixing length theory or SMLT, Ferrari & Nikurashin, 2010; Klocker et al., 2012; Bates et al., 2014; Groeskamp et al., 2020).

Despite the wide use of MLT and SMLT in ocean studies, its applicability to estimating full-depth diffusivity profiles is still unclear. Assumptions about the form of the mixing length for MLT (or unsuppressed mixing length for SMLT) vary from study to study. Some studies assume that the unsuppressed mixing length is depth-independent and is given by either the observed eddy length scale (Bates et al., 2014; Roach et al., 2018) or the local Rossby deformation radius (Groeskamp et al., 2020; Wei & Wang, 2021). This assumption leads to a vertical structure of the diffusivity that is controlled by the vertical structure of the rms eddy velocity and mean flow. Other studies assume that the mixing length does vary in the vertical, and estimate this structure from the Eulerian tracer variance (Cole et al., 2015) or Lagrangian particle dispersion (Chen et al., 2014; Griesel et al., 2014; Wolfram & Ringler, 2017). Reconciling these assumptions requires additional understanding of the vertical structure of eddy properties and a comprehensive comparison of MLT and SMLT against the diagnosed full-depth diffusivity in a broad range of flow regimes.

Additionally, many studies estimate the diffusivity as a scalar, either by assuming that mixing is isotropic along isopycnals (e.g., Adcroft et al., 2019; Redi, 1982) or by only estimating the cross-stream diffusivity (e.g., Ferrari & Nikurashin, 2010; R. Abernathy et al., 2013; Groeskamp et al., 2020). However, isopycnal mixing has been revealed to be broadly anisotropic (e.g., Rypina et al., 2012; Fox-Kemper et al., 2013; S. D. Bachman et al., 2020), and diffusivity is better described by a tensor (Fox-Kemper et al., 2013). Accounting for the anisotropy of the mixing is important for accurate representation of eddy transport in parameterizations (R. D. Smith & Gent, 2004; S. D. Bachman et al., 2020; Stanley et al., 2020). Both Eulerian (S. Bachman & Fox-Kemper, 2013; Fox-Kemper et al., 2013; S. D. Bachman et al., 2015, 2020) and Lagrangian (Chen & Waterman, 2017; Kamenkovich et al., 2015; Rypina et al., 2012; Wolfram et al., 2015) methods have been used to estimate the anisotropy of mixing, and these estimates are usually consistent (Fox-Kemper et al., 2013). A feature of this anisotropy is that mixing is typically much stronger in the direction of the mean flow than across it (S. D. Bachman et al., 2020), which could be due to the enhancement of along-stream mixing by mean flow shear (K. S. Smith, 2005; K. S. Smith, 2007a) or the suppression of cross-stream mixing by eddy propagation relative to the mean flow (Ferrari & Nikurashin, 2010; Klocker et al., 2012). A complete parameterization accounting for this anisotropy requires understanding the scaling of both along- and cross-stream diffusivities.

The vertical structure of tracer diffusivity tensor was recently examined by S. D. Bachman et al. (2020). They proposed an anisotropic parameterization in which the cross-stream diffusivity is equal to the GM diffusivity and ratio of the along-stream to the cross-stream diffusivity is randomly selected from an exponential distribution. This parameterization compared favorably to the vertical profile of the global horizontal average of the diffusivity diagnosed from a high-resolution global ocean model using a multiple tracer inversion method. However, it is unclear how to interpret this comparison, since a horizontally averaged horizontal diffusivity is only meaningful if the diffusivity is spatially constant—multiplying the averaged diffusivity by a gradient (averaged or not) is unlikely to recover the appropriate flux. The vertical structure of eddies is influenced by local baroclinic instability, which varies with location (K. S. Smith, 2007a; K. S. Smith & Marshall, 2009; Tulloch et al., 2011), and the vertical structure of the cross-stream diffusivity is even more complex due to mean flow suppression in regions with differing dynamics (Bates et al., 2014; Cole et al., 2015; Groeskamp et al., 2020; Klocker & Abernathy, 2014). The extent to which extant theories for isopycnal mixing account for this local variability has not been thoroughly studied.

In this study we address whether MLT and SMLT adequately describe the vertical variation and anisotropy of tracer diffusivities and whether the mixing length is depth-independent. This study considers the vertical structure of the isopycnal diffusivity in an idealized basin circulation model that contains multiple gyres, western boundary currents and a circumpolar current like the Antarctic Circumpolar Current. We investigate the vertical profile of diffusivity at various locations that are controlled by different dynamics, in contrast to S. D. Bachman

**Table 1**  
*List of Abbreviations Used in This Paper*

Abbreviation	Description
EKE	Eddy kinetic energy
FVU	Fraction of variance unexplained
GM	Gent and McWilliams (1990) parameterization
MLT	Mixing length theory
MTT	Mixing time theory
MITgcm	Massachusetts Institute of Technology general circulation model
PV	Potential vorticity
Redi	Redi (1982) isopycnal mixing formulation
rms	Root mean square
SLT	Steering level theory
SMLT	Suppressed mixing length theory
SSH	Sea surface height

et al. (2020) who study the profile of globally averaged diffusivity. The 3D diffusivity tensor is diagnosed using the multiple tracer inversion method of S. D. Bachman et al. (2015) to provide a “ground truth” for comparison to scaling theories for the along- and cross-stream diffusivities. This study verifies MLT and SMLT scaling in the upper ocean, but also finds that the mixing regime is distinctly different below the thermocline. Here, the diffusivity scales like the eddy kinetic energy times a depth-independent mixing time. The difference between these mixing regimes is attributed to the dominance by the nonlinear and linear processes in the upper and deep ocean, respectively. We propose an improved theory which combines the effects of both nonlinear and linear mixing processes.

The remainder of the manuscript is organized as follows. Section 2 introduces the mixing theories examined in this study. Section 3 describes the configuration of the numerical model and the multiple tracer inversion method used to diagnose the diffusivity tensor. Section 4 presents the overall properties of the magnitude and orientation of the eigenvalues and eigenvectors of the symmetric part of the diffusivity tensor and their vertical structures. The full-depth scaling of the along- and cross-stream diffusivities (first two eigenvalues) is discussed in Section 5. Section 6 offers a summary and conclusions.

Additional material may be found in appendices. A description of the coherent eddy identification and tracking algorithm is given in Appendix A. Appendix B contains a discussion of the robustness of the diagnosed diffusivity and its ability to reconstruct the observed tracer fluxes, and the geographical distribution of diagnosed mixing length and time scales is given in Appendix C.

## 2. Theoretical Background

### 2.1. The Diffusivity Tensor

The eddy flux of a tracer with concentration  $C$  is often represented using the flux-gradient relationship

$$\overline{u'C'} = -\mathbf{K}\nabla\bar{C}, \quad (1)$$

where  $\mathbf{u}$  is the 3D velocity and  $\mathbf{K}$  is a  $3 \times 3$  diffusivity tensor. The averaging operator  $\overline{(\cdot)}$  is typically a some combination of a space and time mean over the scales of interest and is explicitly defined in Section 3.2. The primes are deviations from this average.

The diffusivity tensor can be decomposed into a sum of a symmetric and antisymmetric parts,

$$\mathbf{K} = \mathbf{S} + \mathbf{A}. \quad (2)$$

The antisymmetric tensor,  $\mathbf{A}$ , gives a skew tracer flux (Griffies, 1998) which behaves like a bolus velocity (Gent et al., 1995). This tensor is commonly used to parameterize the release of mean potential energy by mesoscale

eddies. It is important for ocean dynamics, but has no contribution to the tracer variance budget. In contrast, the symmetric tensor,  $S$ , determines the diffusive transport of tracers and represents an exchange of tracer variance between resolved and unresolved scales. The symmetric tensor reduces (increases) resolved tracer variance if it is positive (negative) definite. Any increase in resolved variance must be local, since eddy diffusion must reduce global tracer variance to balance dissipation. This work aims to study the properties of the tracer diffusion, and so focuses on the symmetric tensor.

The symmetric tensor can be diagonalized as

$$S\boldsymbol{\varphi}_i = \kappa_i\boldsymbol{\varphi}_i, \quad (3)$$

where  $\kappa_i$  ( $i = 1, 2, 3$ ) are the three eigenvalues along the corresponding eigenvectors,  $\boldsymbol{\varphi}_i$  ( $i = 1, 2, 3$ ), which indicate the three orthogonal principal mixing directions. Mixing in the ocean is anisotropic, with the mixing along isopycnals generally much larger than that across isopycnals (Redi, 1982). This means that the largest two eigenvalues,  $\kappa_1$  and  $\kappa_2$ , are expected to represent the mixing along isopycnals, while the smallest eigenvalue,  $\kappa_3$ , represents the mixing across isopycnals. This study focuses on the isopycnal mixing, so will primarily analyze  $\kappa_1$  and  $\kappa_2$ . The isopycnal mixing is itself also often anisotropic in the ocean, with  $\kappa_1$  significantly larger than  $\kappa_2$  (S. D. Bachman et al., 2020). Hereafter,  $\kappa_1$  and  $\kappa_2$  are referred to as the “major” and “minor” diffusivity, respectively.

## 2.2. Mixing Length and Mixing Time Theories

Mixing length theory (MLT, Prandtl, 1925) is a common framework used to understand turbulent mixing. MTL expresses the eddy diffusivity as

$$\kappa_{\text{MLT}} = \Gamma_{\text{MLT}} u_{\text{rms}} L, \quad (4)$$

where  $\Gamma_{\text{MLT}}$  is an order-one nondimensional mixing efficiency,  $u_{\text{rms}}$  is the rms eddy velocity,

$$u_{\text{rms}} = \sqrt{u'^2 + v'^2}, \quad (5)$$

and  $L$  is the “mixing length.” The mixing efficiency,  $\Gamma_{\text{MLT}}$ , is traditionally included in the expression (Equation 4), although it can be absorbed into the definition of the mixing length. We shall adopt this convention and set  $\Gamma_{\text{MLT}} = 1$  in the following. An alternate expression for the eddy diffusivity is due to Taylor (1922), who expressed the diffusivity as

$$\kappa_{\text{MTT}} = \text{EKE} \tau, \quad (6)$$

where EKE is the eddy kinetic energy ( $\text{EKE} = u_{\text{rms}}^2/2$ ) and  $\tau$  is a “mixing time.” The subscript “MTT” stands for “mixing time theory” in analogy to mixing length theory. As with MLT, we have absorbed the (possibly different) mixing efficiency into the definition of  $\tau$ . With this convention for the mixing efficiencies, (Equation 4) and (Equation 6) are equivalent if  $L = u_{\text{rms}}\tau$ .

The mixing lengths and times are, in principle, functions of all three spatial dimensions and time. The eddies responsible for mesoscale mixing are usually coherent and nonlinear in the extratropics (Chelton et al., 2011). These eddies tend to have deep vertical extents (e.g., Zhang et al., 2014), so the distance between coherent eddies, corresponding to the mixing length (Gallet & Ferrari, 2020; Thompson & Young, 2006), is independent of depth—at least in the upper ocean where the eddies are strong (Bates et al., 2014). It is therefore reasonable to expect that the mixing length in Equation 4 is independent of depth where eddies are strong and nonlinear. We refer to the regime where the mixing length is depth independent as the “Prandtl regime.” In this regime, the vertical structure of diffusivity should follow the vertical structure of the rms velocity. We show in Section 5 that the Prandtl regime provides a good description of mixing in our model when eddy mixing is nonlinear in the sense defined in Section 2.4.

Eddy velocities typically decay with depth and at sufficient depth may be weak enough that they no longer produce closed PV contours (Zhang et al., 2014). The flow field then resembles a superposition of linear waves more than a collection of nonlinear eddies. Results from the steering level theory show that the diffusivity associated with linear waves takes the form of the EKE multiplied by a depth-independent time scale (e.g., K. S. Smith & Marshall, 2009; Griesel et al., 2015). In this regime, the diffusivity is given by (Equation 6) with a

depth-independent mixing time and the vertical structure of the diffusivity follows that of the EKE. We refer to this regime as the “Taylor regime” and show in Section 5 that the Taylor regime holds in our model when the eddies are linear, again in the sense defined in Section 2.4. In general, we expect both regimes to coexist at a single geographic location, with the Prandtl regime dominating the upper ocean and a transition with depth to the Taylor regime.

### 2.3. Suppressed Mixing Length/Steering Level Theory

In the presence of strong mean flows, mixing across the mean flow direction is suppressed relative to the predictions of standard MLT and MTT due to the propagation of nonlinear eddies relative to the mean flow (e.g., R. Abernathy et al., 2010; Ferrari & Nikurashin, 2010). Ferrari and Nikurashin (2010) and Klocker et al. (2012) derive a suppressed mixing length theory (SMLT), which accounts for this suppression and show that the cross-stream diffusivity is given by an expression equivalent to

$$\kappa_{\text{SMLT}}(z) = \frac{\kappa_{\text{MLT}}(z)}{1 + \frac{\tau^2}{L^2} [c_w - \bar{u}(z)]^2}, \quad (7)$$

where  $\kappa_{\text{MLT}}$  is the unsuppressed diffusivity given by (Equation 4),  $L$  is the unsuppressed mixing length,  $\tau$  is the eddy decorrelation time scale,  $c_w$  is the zonal eddy phase speed, and  $\bar{u}$  is the zonal mean flow. While the essence of SMLT is captured by (Equation 7 and 4), other versions exist with  $L$  and  $\tau$  replaced by other equivalent dimensional parameters (e.g., a wavenumber and rate rather than a length and time scale) or which differ from (Equation 7 and 4) by the appearance of nondimensional constants of order one.

Steering level theory (SLT), based on linear stability analysis, produces a similar expression for the cross-stream diffusivity (Killworth, 1997; K. S. Smith & Marshall, 2009; Griesel et al., 2015); however, the interpretation is different since the mixing is considered to be due to the growth of linearly unstable waves. The resulting diffusivity,  $\kappa_{\text{SLT}}$ , has a form similar to (Equation 7), except that  $\kappa_{\text{MLT}}$  is replaced by  $\kappa_{\text{MTT}}$ , and the decorrelation time scale,  $\tau$ , corresponds to the growth or decay time scale of linear waves, which is depth-independent (Griesel et al., 2015). Note that the expressions  $\kappa_{\text{SMLT}}$  and  $\kappa_{\text{SLT}}$  are equivalent if  $L = u_{\text{rms}} \tau$  (Ferrari & Nikurashin, 2010; Griesel et al., 2015; Klocker et al., 2012).

Since the cross-stream diffusivity is suppressed by the mean flow, the along-stream diffusivity should be larger than the cross-stream diffusivity. Thus, we expect the symmetric diffusivity tensor,  $\mathbf{S}$ , to be anisotropic with the major diffusivity corresponding to along-stream mixing and minor diffusivity to cross-stream mixing.

### 2.4. A Nonlinearity Parameter

Surface mixing is dominated by nonlinear eddies in the extratropics and by linear waves in the tropics (Klocker & Abernathy, 2014; Klocker et al., 2016). Since eddy amplitudes decay with depth, a similar transition from nonlinear to linear mixing should occur in the vertical. As is discussed in Section 2.2 and 2.3, the vertical structure of diffusivity is likely to be different in the linear and nonlinear regimes, so it is necessary to have a criterion to distinguish these two regimes. A useful nonlinearity parameter is the ratio of the rms eddy velocity to the intrinsic propagation speed of coherent eddies,

$$r = \frac{u_{\text{rms}}}{c}, \quad (8)$$

where

$$c = \sqrt{(\mathbf{u}_{\text{coh}} - \bar{\mathbf{u}}^z)^2} \quad (9)$$

is the intrinsic propagation speed of coherent eddies,  $\mathbf{u}_{\text{coh}}$  is their absolute propagation velocity,  $\bar{\mathbf{u}}^z$  is the depth-averaged mean flow. Chelton et al. (2011), Klocker and Abernathy (2014), and Klocker et al. (2016) propose similar nonlinearity parameters, although the details of the calculation differ slightly from Equation 8 and each other. The eddy propagation speed is obtained from coherent eddies that are identified and tracked from sea surface

height (SSH) snapshots as described in Appendix A. The Doppler shift by the depth-averaged mean flow,  $\bar{u}^z$ , is removed from the total velocity to obtain the intrinsic eddy speed.

The linear and nonlinear regimes are determined by  $r < 1$  and  $r > 1$ , respectively. When  $r > 1$ , the rotational velocity of the eddy is larger than its propagation velocity, so the streamlines within the eddy will close in a frame co-moving with the eddy. If  $r < 1$ , the streamlines within the eddy are not closed and the eddy is wave-like.

### 3. Approach

#### 3.1. Idealized Basin Circulation Model

This study uses an idealized configuration of Massachusetts Institute of Technology general circulation model (MITgcm, J. Marshall, Adcroft, et al., 1997; J. Marshall, Hill, et al., 1997; Campin et al., 2020) used by several previous studies (Wolfe & Cessi, 2009, 2010, 2011; Cessi et al., 2010; Cessi & Wolfe, 2009; Wolfe, 2014; Wolfe et al., 2008). The model is formulated in a two-hemisphere basin on an equatorial  $\beta$ -plane ( $\beta = 2.3 \times 10^{-11} \text{ m}^{-1} \text{ s}^{-1}$ ) with a flat bottom. The model domain has width  $W = 2,440 \text{ km}$  in zonal direction, length  $L_y = 9,880 \text{ km}$  in meridional direction and a uniform depth  $H = 2,440 \text{ m}$ , with no-slip vertical walls on the boundaries, except for the southern eighth of the domain, where the flow is zonally reentrant (Figure 1). The horizontal resolution is  $5.4 \text{ km}$ . The vertical grid spacing varies from  $13 \text{ m}$  at the surface to  $274 \text{ m}$  at the bottom with a total of 20 vertical levels.

The model is forced by zonally uniform zonal winds (orange line in Figure 1c) and a relaxation to a zonally uniform surface temperature distribution (blue line in Figure 1c), an idealization of the forcing in the Atlantic Ocean. The dissipation is provided by the horizontal Laplacian viscosity ( $A_h = 12 \text{ m}^2 \text{ s}^{-1}$ ), horizontal biharmonic viscosity ( $A_4 = 9 \times 10^8 \text{ m}^4 \text{ s}^{-1}$ ), vertical viscosity ( $A_v = 3 \times 10^{-4} \text{ m}^2 \text{ s}^{-1}$ ), and linear bottom drag ( $r_d = 1.1 \times 10^{-3} \text{ m s}^{-1}$ ). Buoyancy is a linear function of temperature only, which is advected using a seventh-order monotonicity-preserving scheme (Daru & Tenaud, 2004) and diffused with a constant isotropic diffusivity ( $\kappa = 4.9 \times 10^{-5} \text{ m}^2 \text{ s}^{-1}$ ) in both horizontal and vertical directions. The model starts from equilibrated fields from previous studies (e.g., Wolfe & Cessi, 2009, 2010). The velocity, temperature and eddy statistics are averaged online and saved every half year for 30 years. Figure 1a shows the mean surface flow fields in the model. The model contains multiple gyres, boundary currents, and a zonally reentrant channel flow analogous to the Antarctic Circumpolar Current.

Figure 2 compares the model horizontal resolution to the zonally averaged Rossby deformation radius of the first baroclinic mode,  $L_d$ , calculated by solving a numerical Sturm-Liouville problem. The horizontal grid spacing is less than half of  $L_d$ , except near the northern boundary and in the zonally reentrant channel. Consistent with the results of (Tulloch et al., 2011), the length scale of the most unstable mode of baroclinic instability in the channel is about two times  $L_d$  (not shown), which is resolved by the model, except very near the southern boundary. Mesoscale eddies are therefore sufficiently resolved in the northern half of the channel, although we acknowledge that higher resolution would be ideal. Figure 1b gives a snapshot of the surface vorticity normalized by the local Coriolis frequency (i.e., the local Rossby number) and SSH anomaly fields, which shows that rich eddy fields are resolved in most parts of the model domain, including the channel. The Rossby number is much less than one in most of the domain, except in the tropics. Fine scale features with large Rossby numbers appear at the boundary of the tropics, which suggests that submesoscale processes are marginally resolved there.

The use of a  $\beta$ -plane is primarily for the convenience of Cartesian coordinates and may appear to restrict the dynamical regime to be either  $\beta$ -dominated or shear-dominated (depending on the value of  $\beta$ ). However, while the dimensional value of  $\beta$  is fixed in the  $\beta$ -plane approximation, the dynamical impact of  $\beta$  is measured by the Charney-Green number (Charney, 1947; Green, 1960). This number measures the relative importance of PV gradients due to  $\beta$  and vertical shear and can be written as

$$\beta^* = \frac{\beta L_d}{\sigma_E}, \quad (10)$$

where  $L_d$  is the Rossby deformation radius and  $\sigma_E$  is the Eady growth rate, estimated as

$$\sigma_E = f \sqrt{\frac{1}{H} \int_{-H}^0 \frac{|\bar{u}_z|^2}{N^2} dz}, \quad (11)$$



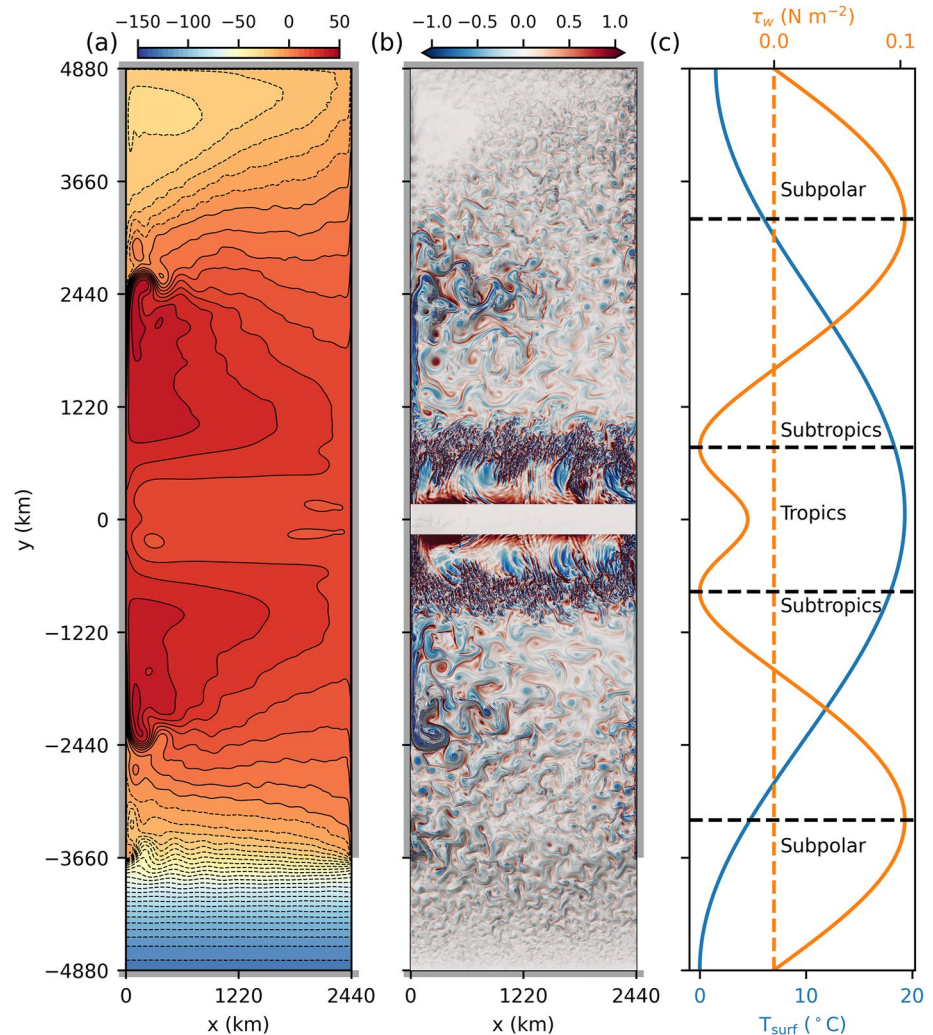


**Figure 1.** (a) 30-year mean sea surface height (SSH) field in centimeters from the idealized eddy-resolving basin model. The contour interval is 5 cm and negative contours are dashed. (b) Snapshot of the instantaneous surface layer vorticity divided by the Coriolis frequency,  $f$ , (colors) and sea surface height (shading) from the same model. The shading around the edges of (a) and (b) are the walls on the boundary. There is a circumpolar channel in the southernmost eighth of the domain. (c) Zonal wind stress,  $\tau_w$ , (orange line) and surface relaxation temperature,  $T_{surf}$ , (blue line) as functions of  $y$ . The orange dashed line gives the zero of  $\tau_w$ . Black dashed lines divide the domain into different circulation regimes, marked by the black labels.

where  $|\bar{u}_z|$  is the magnitude of the mean vertical shear (K. S. Smith, 2007b) and  $N$  is the Brunt-Väisälä frequency estimated from the mean buoyancy field, where the mean is a 20-year average. Both of  $L_d$  and  $\sigma_E$  vary by more than an order of magnitude within the model domain. The resulting Charney-Green number varies from much larger than one in the tropics to much less than one at high latitudes (orange line in Figure 2), reflecting  $\beta$  dominance at low latitudes and shear dominance at high latitudes. Thus, while  $\beta$  is fixed, the *effective*  $\beta$  varies over a wide range.

### 3.2. Diagnosing the Diffusivity Tensor Based on a Tracer-Based Inversion Method

The nine-component diffusivity tensor is diagnosed using the tracer-based inversion method of S. D. Bachman et al. (2015), (2020), which is used as the “ground truth” to test against the existing scaling theories. An advantage of this method is that it accounts for the anisotropy of eddy diffusion by diagnosing each component of a diffusivity tensor using multiple tracers, rather than simply calculating a scalar diffusivity based on the flux-gradient

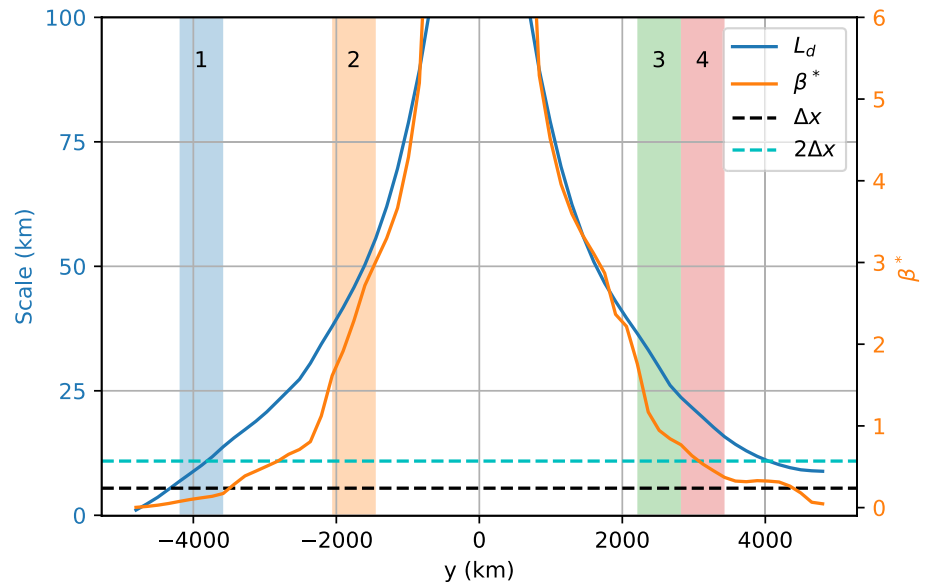


**Figure 2.** Zonal average of the Rossby deformation radius (blue solid line) and the Charney-Green number,  $\beta^*$ , (orange solid line) as a function of  $y$ . Black and cyan dashed lines indicate one and two times the model's horizontal grid spacing. Blue, orange, green and red shadings indicate the locations where we analyze the vertical profiles of diffusivities in Figure 5.

relationship of a single tracer. At least three different tracers are required to uniquely solve for the nine components of the diffusivity tensor, but to reduce the noise and bias due to the choice of tracers we use more than three tracers to overdetermine the diffusivity tensor and solve for the diffusivity using a least squares method (S. D. Bachman et al., 2015, 2020).

A total of 27 passive tracers,  $C_\alpha$ , are advected with the velocity field of the model according to

$$\frac{DC_\alpha}{Dt} = \lambda_\alpha (C_\alpha^0 - C_\alpha), \quad (12)$$

where  $\lambda_\alpha$  is the relaxation rate and  $C_\alpha^0$  is the initial condition of  $\alpha^{\text{th}}$  tracer. The 27 tracers are divided into 3 sets; each set is relaxed to the initial conditions with relaxation time scales of 1 year for tracers 1–9, 3 years for tracers 10–18, and 9 years for tracers 19–27. Tracers in each set are initialized with 9 different conditions,

$$\begin{aligned} C_{1,10,19}^0 &= \frac{y}{L_y}, & C_{2,11,20}^0 &= \sin \frac{\pi y}{L_y}, & C_{3,12,21}^0 &= \cos \frac{\pi y}{L_y}, \\ C_{4,13,22}^0 &= \sin \frac{2\pi x}{W}, & C_{5,14,23}^0 &= \cos \frac{2\pi x}{W}, & C_{6,15,24}^0 &= \sin^2 \frac{\pi x}{W}, \\ C_{7,16,25}^0 &= \frac{H-2z}{H}, & C_{8,17,26}^0 &= \cos \frac{\pi z}{H}, & C_{9,18,27}^0 &= \sin \frac{2\pi z}{H}, \end{aligned} \quad (13)$$

These tracer distributions are chosen because they are simple and linearly independent; they are similar to those chosen by S. D. Bachman et al. (2020). The diagnosed diffusivity is not sensitive to the details of the tracer initial conditions provided sufficient tracers are used. The linear independence of tracers is maintained by the relaxation in Equation 12. Different relaxation rates will cause the tracers that have the same initial distributions to misalign relative to each other during the simulation, so that tracers with identical initial conditions but different relaxation rates will, in general, have linearly independent equilibrium distributions.

Tracer concentrations and fluxes equilibrate after approximately 10 years and are then time-averaged online over 20 years. The time-averaged quantities are then coarsened onto a 152 km horizontal grid by spatial averaging and gradients calculated on the coarsened grid. The coarsening scale is chosen because it is coarse enough to separate the mesoscale from the large scale poleward of the tropics but still fine enough to capture spatial variability. The specific value of 152 km is an even number of uncoarsened grid cells (28) and exactly divides the domain into  $64 \times 16$  coarsened grid cells in the meridional and zonal directions, respectively. Coarsening scales of 76 and



304 km were also tested and gave similar magnitudes, spatial variations, and probability distributions of diffusivities as the 152 km case.

The 3D eddy diffusivity tensor,  $\mathbf{K}$ , is diagnosed by inverting the flux-gradient relationship

$$\mathbf{K} = -\overline{u' C'} [\nabla \bar{C}]^\dagger, \quad (14)$$

where  $C$  is a row vector of the 27 tracers,  $\overline{(\cdot)}$  is a 20-year and 152-km spatial average,  $(\cdot)'$  is the deviation therefrom, and  $(\cdot)^\dagger$  denotes the Moore-Penrose pseudoinverse (Moore, 1920; Penrose, 1955). The pseudoinversion solves for  $\mathbf{K}$  in a least squares sense while automatically removing linearly dependent combinations of tracers. Using a large number of tracers guards against rank-deficiency when tracer distributions “accidentally” align and significantly reduces the dependence of the diffusivity on the choice of a particular set of tracers (S. D. Bachman et al., 2015). We show in Appendix B that the diagnosed diffusivity is able to accurately reconstruct local eddy tracer fluxes, including those tracers that are not used to determine the diffusivity. This means that, unlike the methods of Kamenkovich et al. (2021) and Sun et al. (2021), pseudoinversion produces a diffusivity tensor that is generic; that is, it is not strongly dependant on the tracers used to diagnose it.

## 4. Structure of the Symmetric Diffusivity Tensor

### 4.1. Anisotropy and Orientation of the Mixing

The horizontal distribution of the three eigenvalues of the symmetric diffusivity tensor,  $\mathbf{S}$ , at 138 m depth is shown in Figure 3. The first two eigenvalues,  $\kappa_1$  and  $\kappa_2$ , are nearly horizontal and much larger than the third eigenvalue,  $\kappa_3$ , which is almost vertical. Figure 4a shows the histogram for the angles between the direction of each eigenvector and the buoyancy gradient normalized by the angle between the buoyancy gradient and the vertical direction. This normalization is necessary because isopycnal slopes are themselves small, so small

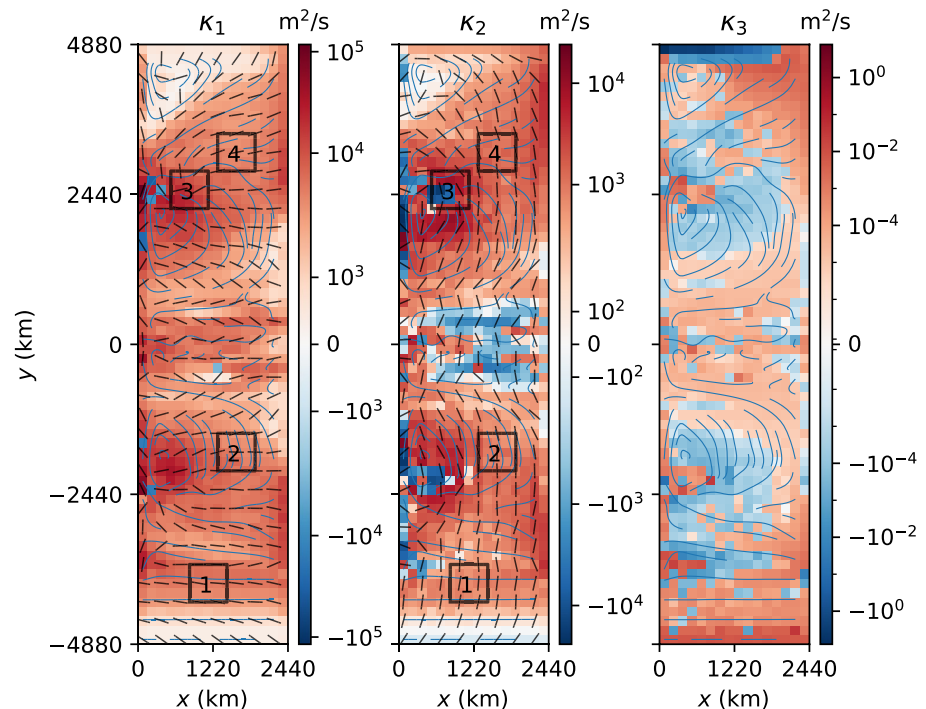


**Figure 3.** Eigenvalues for the symmetric part of the diffusivity tensor at 138 m depth as an example. Black lines indicate the horizontal direction of the corresponding eigenvectors. The last eigenvalue  $\kappa_3$  is almost vertical, so the horizontal components of its eigenvector are small. Blue lines are the mean flow streamlines. Black boxes labeled by numbers are the regions where the vertical structures of the diffusivities are analyzed.

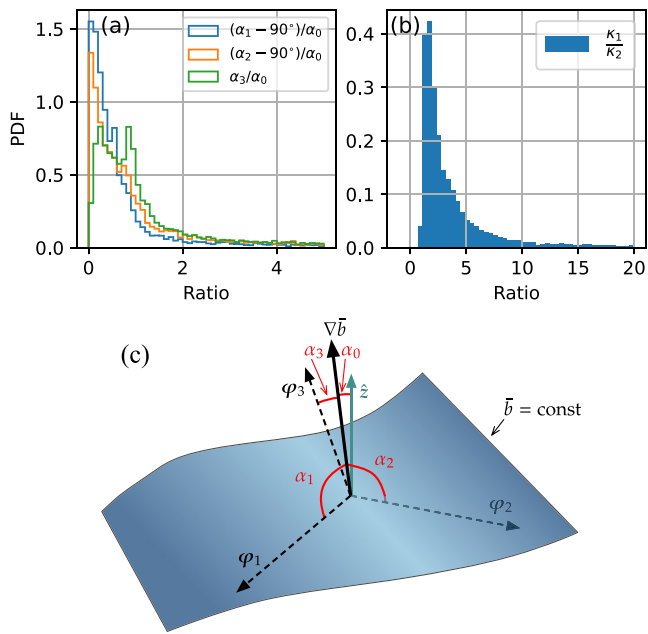


**Figure 4.** (a) Probability distribution function of the angles,  $\alpha_{1,2,3}$ , between the three eigenvectors,  $\varphi_{1,2,3}$ , and the mean buoyancy gradient,  $\nabla \bar{b}$ , normalized by the angle,  $\alpha_0$ , between the mean buoyancy gradient and the vertical direction,  $\hat{z}$ , with  $(\alpha_{1,2} - 90^\circ)/\alpha_0$  in blue and orange, respectively, and  $\alpha_3/\alpha_0$  in green. Small values of  $(\alpha_{1,2} - 90^\circ)/\alpha_0$  indicate that the eigenvectors are nearly perpendicular to the mean buoyancy gradient. (b) Probability distribution function of the ratio of the major to the minor diffusivities. (c) Schematic for the angles between three eigenvectors and the mean buoyancy gradient. The blue curved surface indicates an mean isopycnal surface and the solid black line indicates the mean buoyancy gradient. The angle,  $\alpha_0$ , between the mean buoyancy gradient and the vertical direction (solid green arrow) is indicated in red. The dashed black lines indicate the directions of the three eigenvectors,  $\varphi_{1,2,3}$ , with the angles between these and the buoyancy gradient,  $\alpha_{1,2,3}$ , indicated in red. Note that the mixing directions are  $\pm\varphi_i$  since eigenvectors are sign invariant; reversing the direction of  $\varphi_i$  does not change the angle  $\alpha_i$ .

absolute angles do not necessary imply that the mixing directions are aligned with isopycnals (but small normalized angles do). The eigenvectors and their angles with the buoyancy gradient are shown in the schematic in Figure 4c. The directions of  $\kappa_1$  and  $\kappa_2$  are nearly along the isopycnals (i.e., are epicycnal) at a majority of grid points, while the direction of  $\kappa_3$  is predominantly diapycnal. Values in the tail of the distribution are primarily from the deep tropics and regions of active convection. These places are weakly stratified and isopycnal slopes are difficult to determine numerically.

Epicycnal diffusion by mesoscale eddies, represented by  $\kappa_1$  and  $\kappa_2$ , plays an important role in tracer transport along isopycnals, which have been widely investigated in oceanic observations (e.g., Stammer, 1998; Zhurbas & Oh, 2003, 2004; J.; Marshall et al., 2006; R. P.; Abernathy & Marshall, 2013; Cole et al., 2015; Groeskamp et al., 2017; Roach et al., 2018) and is also the focus of this study. Diapycnal mixing, although important, is more likely to be induced by submesoscale, fine-scale, or microscale processes which are not resolved in this model. The diapycnal diffusivity,  $\kappa_3$ , is therefore not the focus in this study since it excludes these important contributions.

The magnitude of  $\kappa_1$  is 2–3 times larger than  $\kappa_2$  on average (Figure 4b), indicating that the isopycnal mixing is anisotropic. Hereafter  $\kappa_1$  and  $\kappa_2$  will be denoted as the major and minor isopycnal diffusivities, respectively. The horizontal direction of the major diffusivity,  $\kappa_1$ , is primarily aligned with the mean flow, with an exception in the subtropical gyres, while the direction of the minor diffusivity  $\kappa_2$  is primarily across the mean flow, orthogonal to the major diffusivity (Figure 3; see also Figure 6). Both the major and minor diffusivities are occasionally negative—this primarily occurs in the equatorial current regions, western boundary current and its extensions, and the northwest corner of the circumpolar current (Figure 3). In these regions the advection of tracer variance by mean flow is significant, which can allow upgradient eddy tracer fluxes. This can be understood by considering the tracer variance budget,

$$\frac{\partial}{\partial t} \frac{\overline{C'^2}}{2} + \nabla \cdot \left( \mathbf{u} \frac{\overline{C'^2}}{2} \right) + \overline{\mathbf{u}'C'} \cdot \nabla \bar{C} = \overline{C'D'} + \overline{C'S'}, \quad (15)$$

where  $\overline{C'^2}/2$  is the tracer variance,  $D$  represents dissipation, and  $S$  represent sources (i.e., relaxation). Assuming a statistically steady state with weak relaxation and invoking the flux-gradient parameterization of the eddy fluxes, the tracer variance budget becomes

$$\nabla \cdot \left( \mathbf{u} \frac{\overline{C'^2}}{2} \right) - \nabla \bar{C} \cdot \mathbf{S} \cdot \nabla \bar{C} \approx \overline{C'D'} < 0, \quad (16)$$

where the less-than sign emphasizes that dissipation is a sink of tracer variance. The sign of the diagraphic flux term,  $\nabla \bar{C} \cdot \mathbf{S} \cdot \nabla \bar{C}$ , depends on the signs of the eigenvalues of  $\mathbf{S}$  (i.e., the diffusivities). This term is positive-(negative-) definite if all the diffusivities are positive (negative); otherwise it is sign-indefinite. If advection of tracer variance [first term on the LHS of Equation 16] is negligible or divergent, the cross-gradient term—and thus the diffusivities—must be positive to balance dissipation. On the other hand, significantly convergent variance advection can overwhelm dissipation and negative diffusivities are required to balance the sum of advection and dissipation.

Note that S. D. Bachman et al. (2020) also find negative diffusivities in energetic regions unless they constrain their inversion to only produce positive diffusivities. There is no physical reason to insist that eddy diffusivities be positive and constraining them to be so degrades the ability of the diffusivities to reconstruct the modeled

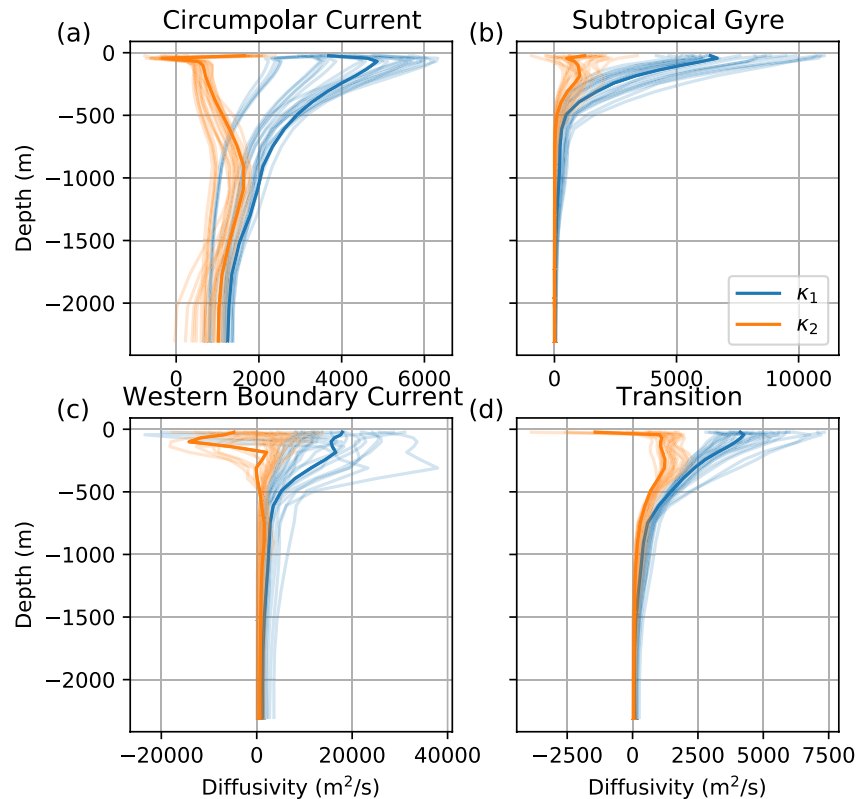


**Figure 5.** Vertical profiles of the isopycnal diffusivity in the four regions indicated by the black boxes in Figure 3. The four regions labeled 1, 2, 3, and 4 in Figure 3 are located in the (a) circumpolar current, (b) subtropical gyre, (c) western boundary current, and (d) transition between the subtropical and subpolar gyres, respectively. Blue and orange lines give the vertical profiles of the major diffusivity,  $\kappa_1$ , and minor diffusivity,  $\kappa_2$ , respectively, at all grid points in the four regions. The thick lines highlight the profiles at the geographic center of the four regions; these profiles are used to illustrate predictions for their vertical structure shown in Figures 8 and 11.

tracer fluxes, so we have avoided implementing such a constraint. On the other hand, we avoid considering the negative diffusivities in detail due to a relative lack of theoretical results for negative diffusivities on which base our analysis. Examination of the negative diffusivities will be pursued in the future work.

#### 4.2. Vertical Structure

The vertical structure of the isopycnal diffusivity is less well understood than the horizontal structure due to the sparsity of full-depth observations (Groeskamp et al., 2020). This study seeks to relate the vertical structure of the diffusivity to the dynamical properties in four typical regions with different dynamics: the circumpolar current, subtropical gyre, western boundary current, and transition between subtropical and subpolar gyres (shown by the black boxes labeled 1, 2, 3, and 4, respectively, in Figure 3). The vertical profiles of the first two eigenvalues are analyzed in  $600 \times 600$  km boxes (black boxes in Figure 3) in the four regions.

The vertical structures of the magnitude of  $\kappa_1$  and  $\kappa_2$  in these four regions are shown in Figure 5. The vertical structures of diffusivities are similar within each region, except in the western boundary current where the local variation is large. The horizontal distribution of diffusivities in the western boundary current extension is complicated by the stability of the jets, wave radiation and formation of recirculations, which can lead to both positive and negative diffusivities (Chen & Waterman, 2017; Waterman & Jayne, 2011). For example, the eddy diffusivity is positive in the upstream part of the extensions (which stabilizes the jet) and becomes negative further downstream, driving the flanking recirculations (Waterman & Jayne, 2011). A detailed study on the mean flow dynamics and tracer variance budget in this region is, however, out of the scope of the current work.

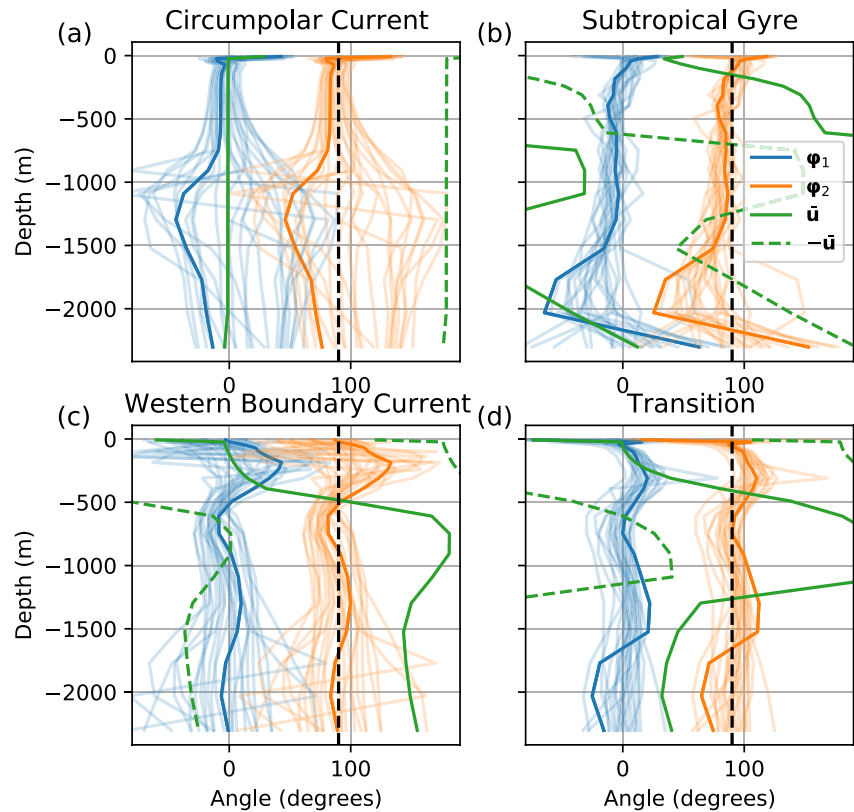


**Figure 6.** As in Figure 5, but for the angles of the eigenvectors  $\varphi_1$  (blue line),  $\varphi_2$  (orange line) and the mean flow (green solid line) in degrees relative to the zonal direction. The direction opposite the mean flow (green dashed line) is also compared with the principal mixing directions since the eigenvectors are invariant under  $180^\circ$  rotations. The black dashed line indicates the meridional direction.

The magnitude of  $\kappa_1$  is generally several times larger than  $\kappa_2$ , especially near the surface (Figure 5), indicating strong anisotropy there. The major diffusivity,  $\kappa_1$ , decreases monotonically with depth, except in some levels near the surface, while the minor diffusivity,  $\kappa_2$ , tends to have a subsurface maximum, which can reach to 1,000 m in the circumpolar current and is shallower than 500 m depth in the other three regions. The cross-stream diffusivity in the Southern Ocean has also been observed to have a subsurface maximum (K. S. Smith & Marshall, 2009; R. Abernathy et al., 2010), which is explained to be due to the suppression of mixing by the mean flow (Chapman & Sallée, 2017; Ferrari & Nikurashin, 2010; Klocker et al., 2012; Wolfram & Ringler, 2017). Since the direction of the minor diffusivity,  $\kappa_2$ , is mostly across the mean flow as well, we expect the vertical structure of  $\kappa_2$  is affected by the mean flow suppression, which will be tested in the following section. The major diffusivity,  $\kappa_1$ , on the other hand, is mostly along the mean flow direction, which has been shown to be less impacted by the mean flow suppression than the cross-stream diffusivity (Chen et al., 2014; Griesel et al., 2014; Riha & Eden, 2011).

Figure 6 shows the vertical structure of the orientation of  $\varphi_1$  and  $\varphi_2$  in the four regions. The direction of  $\varphi_1$  ( $\varphi_2$ ) is generally along the zonal (meridional) direction in the upper levels of the four regions, and it is almost along (across) the direction of the mean flow above 1,000 m in the four regions. The surface meridional mean flow is dominated by the Ekman flow, which is confined in the first vertical grid cell in this model (Figure 7). Rypina et al. (2012) found that the Ekman flow can reduce the anisotropy of mixing by reducing the eddy spreading along mean flow, but this impact is secondary compared with the mixing by the surface geostrophic flow. We expect this impact of the Ekman flow should—like the flow itself—be confined in the first layer in this model. In the deep levels  $\varphi_1$  is less aligned with the mean flow, perhaps because the mean flow is weak at depth (Figure 7) and the interior PV gradient plays a more important role in the mixing direction (S. D. Bachman et al., 2020). In the subtropical gyre the direction of mean flow is not well-defined, because of the strong veering of the mean flow with depth (Figure 7). In the circumpolar current the mixing directions veer from the mean flow direction at around 1,000 m where magnitude of the major and minor diffusivities are similar. That means the mixing is

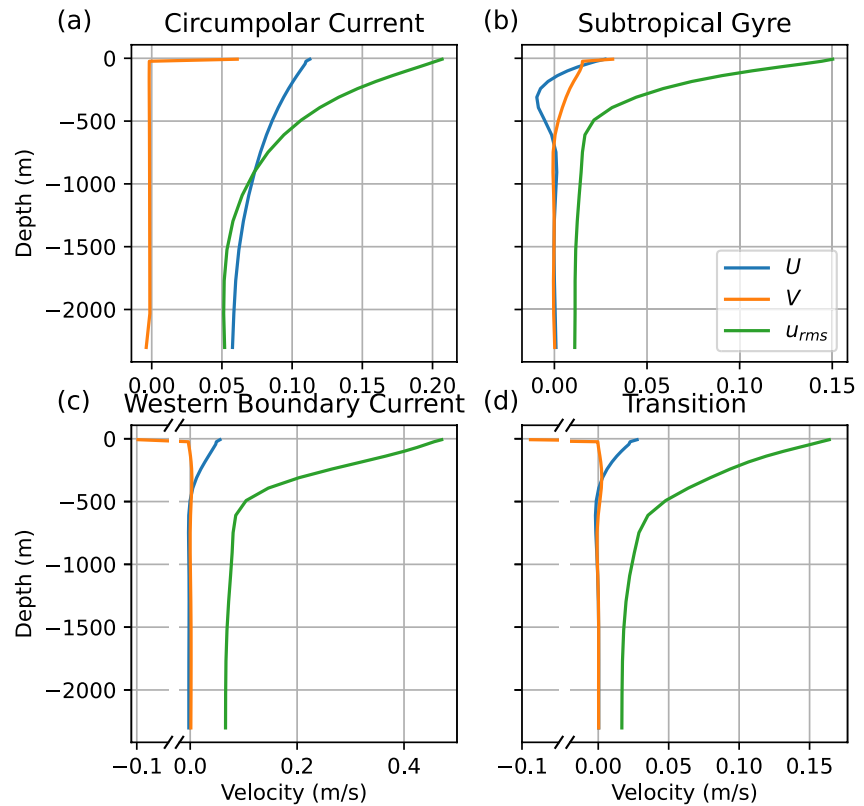


**Figure 7.** Vertical structure of the zonal (blue line) and meridional (orange line) mean flow velocity averaged over 20 years and horizontally averaged over the same four regions as in Figure 5. Note that a portion of the abscissa, from  $-0.041$  and  $-0.074$  to  $-0.02$  m/s, are cut out in (c) and (d), respectively, to keep small variations of mean flow visible. The surface meridional velocity is large because the surface meridional flow is dominated by Ekman flow and the Ekman layer is confined in the first vertical grid cell in this model.

nearly isotropic at those depths and the mixing directions become arbitrary. This is likely because the mean flow becomes weak at depth and no longer acts to suppress the cross-stream diffusivity.

## 5. What Determines the Vertical Structure of the Diffusivities?

The diffusivities,  $\kappa_1$  and  $\kappa_2$ , determine tracer mixing along isopycnals, which has important impacts on the mean flow (Fox-Kemper et al., 2013; Bates et al., 2014; Chapman & Sallée, 2017; S. D. Bachman et al., 2020). Understanding the physical mechanism that gives rise to the anisotropy and vertical structure of these diffusivities can guide their parameterization in coarse-resolution models. Here we test the vertical structure of  $\kappa_1$  and  $\kappa_2$  against the existing theories. Specific interest is attached to the source of the anisotropy of the isopycnal mixing and the applicability of MLT and SMLT to the full-depth diffusivities.

### 5.1. Source of the Anisotropy

The major diffusivity,  $\kappa_1$ , is generally along the mean flow and is several times larger than the minor diffusivity,  $\kappa_2$ . What is the source of this anisotropy? Extant theories often suppose that along-stream mixing is dominated by shear-dispersion (Taylor, 1953; Young et al., 1982; K. S. Smith, 2005, 2007a), which leads to the shear-dispersion diffusivity

$$\kappa_{SD} \sim \frac{U^2 l_s^2}{\kappa_{\perp}}, \quad (17)$$



where  $U$  is a scale for the mean flow,  $l_s$  is the scale of the mean flow shear, and  $\kappa_{\perp}$  is the cross-stream diffusivity. However, attempts to use Equation 17 to scale  $\kappa_{\perp}$  did not show good agreement (not shown), which suggests that shear dispersion is not playing a strong role in determining  $\kappa_{\perp}$ .

Another possible source of anisotropy is the suppression of cross-stream mixing by the mean flow, which is explained by SMLT and SLT (e.g., K. S. Smith & Marshall, 2009; Ferrari & Nikurashin, 2010; Klocker et al., 2012). Both SMLT and SLT construct the cross-stream diffusivity as a background eddy diffusivity times a suppression factor,  $F_s$ , defined as

$$F_s(z) = \frac{1}{1 + \frac{\tau^2}{L^2} [c_w - \bar{u}(z)]^2}, \quad (18)$$

which estimates the suppression of diffusivity due to the propagation of nonlinear eddies relative to the mean flow, where  $L$ ,  $\tau$ ,  $c_w$ , and  $\bar{u}$  are as in Equation 7. Here  $\bar{u}$  is obtained from the model ( $\bar{u}$  is simply taken as the zonal mean flow because we find that the suppression factor containing the zonal mean flow dominates over that containing the meridional mean flow since the zonal eddy phase speed is much stronger than the meridional speed), and  $c_w$  is estimated following Klocker and Marshall (2014):

$$c_w = \bar{u}^z - \beta L_d^2, \quad (19)$$

where  $\bar{u}^z$  is the depth-averaged zonal mean flow.

The diagnosed cross-stream diffusivity,  $\kappa_2$ , is compared with the suppressed along-stream diffusivity,  $\kappa_1 F_s$ . The fit of  $\kappa_1 F_s$  to the profiles of  $\kappa_2$  at the center of the four regions is shown by the orange solid line in Figure 8, where the  $\tau/L$  in Equation 18 is treated as a single depth-independent parameter following Bates et al. (2014) and obtained by least squares fitting, which minimizes the vertical integral of the squared difference between  $\kappa_1 F_s$  and  $\kappa_2$  in each profile. The minimization algorithm we use is the Trust Region Reflective algorithm, implemented by the Optimize function in SciPy version 1.7.3. The bounds for the fitting parameters are set to be between 0 and infinity. The suppressed major diffusivity,  $\kappa_1 F_s$ , captures the vertical maximum and variation of  $\kappa_2$  well in these regions, except in the western boundary current where negative values of diffusivity spoil the scaling.

The goodness of fit for the scaling theory is quantified by the fraction of variance unexplained (FVU),

$$\text{FVU} = \frac{\int_{-H}^0 (\kappa_{\text{obs}} - \kappa_{\text{fit}})^2 dz}{\int_{-H}^0 (\kappa_{\text{obs}} - \bar{\kappa}_{\text{obs}}^z)^2 dz}, \quad (20)$$

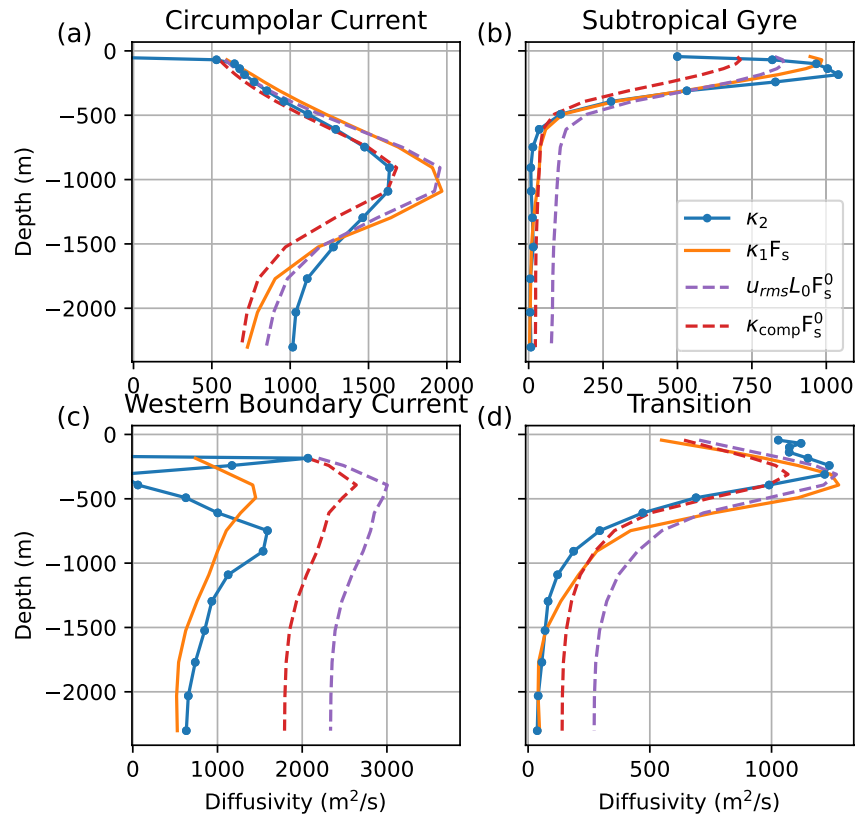
where  $\kappa_{\text{obs}}$  is the diagnosed diffusivity,  $\bar{\kappa}_{\text{obs}}^z$  is the vertical average of  $\kappa_{\text{obs}}$ , and  $\kappa_{\text{fit}}$  is the prediction by the scaling theory. A smaller FVU indicates a better fit. If FVU is larger than one, that means  $\kappa_{\text{fit}}$  explains less of the vertical variation of  $\kappa_{\text{obs}}$  than the mean of  $\kappa_{\text{obs}}$ .

Figure 9a shows the distribution of the FVU evaluated for the vertical profile of  $\kappa_2$  at each coarsened grid cell. The formula  $\kappa_1 F_s$  provides a good model for  $\kappa_2$  in most of the extra-tropics except near the boundaries. This suggests that the along- and cross-stream diffusivities satisfy the same scalings, with the difference due to the suppression of cross-stream mixing by the mean flow. The anisotropy of the diagnosed isopycnal diffusion thus appears to be primarily due to the mean flow suppression effect.

## 5.2. Mixing Regime Transition With Depth

Section 5.1 shows that the minor diffusivity,  $\kappa_2$ , can be reconstructed from the major diffusivity,  $\kappa_1$ , after accounting for the mean flow suppression effect. The vertical profile of the mean flow can be diagnosed from hydrography or the resolved flow in coarse resolution models, so the remaining unknown is what determines the vertical structure of the major diffusivity.

As discussed in Section 2.2, mixing is likely controlled by different dynamics at different depths if there is a transition from a nonlinear to a linear regime with depth. The nonlinear and linear regimes can be distinguished by whether the nonlinearity parameter  $r$  defined by Equation 8 is greater or less than unity, respectively. Figure 10 shows the vertical variation of  $r$  in the four regions. Also shown for reference is the stratification scale depth,  $h_0$ ,



**Figure 8.** Scaling of the minor diffusivity,  $\kappa_2$  (blue solid line with dots), at the center of the four regions, shown in Figure 5. Orange lines show the fit for the vertical structure of  $\kappa_2$  to the formula of  $\kappa_1 F_s$  ( $F_s$  expressed in Equation 18). Note that the negative values of the diffusivity are excluded from the fit. The purple and red dashed lines show the estimate with SMLT,  $u_{rms} L_0 F_s^0$ , and the suppressed composite scaling,  $\kappa_{comp} F_s^0$ , respectively, where the mixing length and time scales in the suppression factor  $F_s^0$  is estimated as the energy containing scale,  $L_0$ , and a uniform decay time scale,  $\tau_0 = 24$  days, respectively—see Section 5.4.

$$h_0 = \frac{\int z N^2 dz}{\int N^2 dz}, \quad (21)$$

which is a proxy for the base of the thermocline. The scale depth would be equal to the e-folding depth if the stratification were exponential. Outside of the circumpolar current, the parameter  $r$  decays rapidly above the thermocline and then asymptotes to a value less than 1 below thermocline. In the circumpolar current,  $r > 1$  over the full depth. This indicates that eddies in the circumpolar current are nonlinear over whole water column, while in the other three regions nonlinear dynamics dominates above the thermocline and linear dynamics is more significant below it. Parameterizations of full-depth mixing should account for this regime transition to produce the correct vertical structure of mixing.

The major diffusivity,  $\kappa_1$ , at the center of the four regions is shown in Figure 11. The diffusivity is fit to the Prandtl regime (Equation 4) and Taylor regime (Equation 6) over depths where the nonlinearity parameter is larger and smaller than unity, respectively. The green and orange solid lines in Figure 11 show the fits for the Prandtl and Taylor regimes, respectively. The Prandtl regime closely captures the vertical variation of  $\kappa_1$  over full depth in the circumpolar current, while in the three basin regions, the Prandtl regime works well in the upper several hundred of meters where the flow is nonlinear but overestimates the diffusivity at depth. The Taylor regime captures the vertical structure of  $\kappa_1$  well in the deep ocean in the three basin regions, where the flow is linear. Although the deep diffusivity is small, the mixing time scale is comparable to the mean flow advection time scale, so the mixing can still significantly impact deep water masses and circulation on climatological timescales. These results show that the mixing regime transitions from the Prandtl regime to the Taylor regime from the

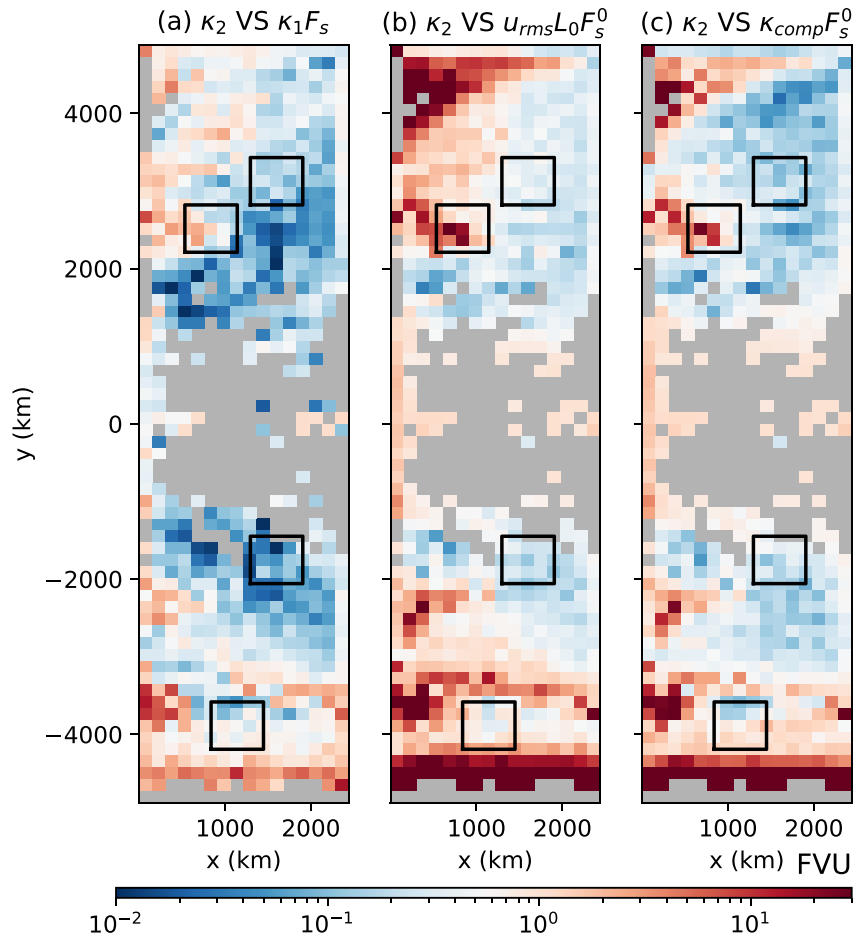


**Figure 9.** Fraction of variance unexplained (FVU) (20) for the comparison between the vertical profile of the minor diffusivity,  $\kappa_2$ , and (a) the fit of the formula of  $\kappa_1 F_s$  to  $\kappa_2$ , (b)  $u_{rms} L_0 F_s^0$ , where  $F_s^0$  is described by (Equation 26), and (c)  $\kappa_{comp} F_s^0$ , where  $\kappa_{comp}$  is defined in Equation 25. Black boxes are the regions where the vertical structure of the diffusivity is analyzed in Figure 8. Note that regions with negative diffusivities covering more than 1,000 m are masked with gray color. Negative diffusivities are also excluded from the fit and calculation of FVU.

upper to deep ocean in the three basin regions, because of the dominance by nonlinear eddies and linear waves in the upper and deep ocean, respectively.

To further verify the correspondence between the Prandtl (Taylor) regime and nonlinear (linear) regime, the vertical profile of the major diffusivity at each grid point is divided into two segments with  $r > 1$  and  $r < 1$  and compared to the Prandtl and Taylor regimes, respectively. Figures 12a and 12b show the misfit ratio, FVU, for the fit of  $\kappa_1$  at depths where  $r > 1$  to the Prandtl regime (Equation 4) and the fit at depths where  $r < 1$  to the Taylor regime (Equation 6), respectively. In the circumpolar current,  $r$  is larger than 1 over almost full depth, while in the tropics,  $r$  is smaller than 1 over full depth (regions where no coherent eddy is detected are regarded to be linear over full depth). The FVU for the fits of both (Equation 4) and (Equation 6) is smaller than 0.5 in most regions, meaning that the mixing in nonlinear regime is well-described by the Prandtl regime and the mixing in linear regime is well-described by the Taylor regime. The mixing regime transitions from Prandtl to Taylor regimes from the upper to deep ocean in the subtropics and midlatitudes where eddies are nonlinear and linear in the upper and deep ocean, respectively. In the circumpolar current, where eddies are nonlinear over full depth, the mixing is well-described by the Prandtl regime. In the tropics, where eddies are linear over full depth, the Taylor regime works well. Large values of FVU are found along the western and southern boundaries, which might be related to the eddy decay due to the lateral friction at the boundary.

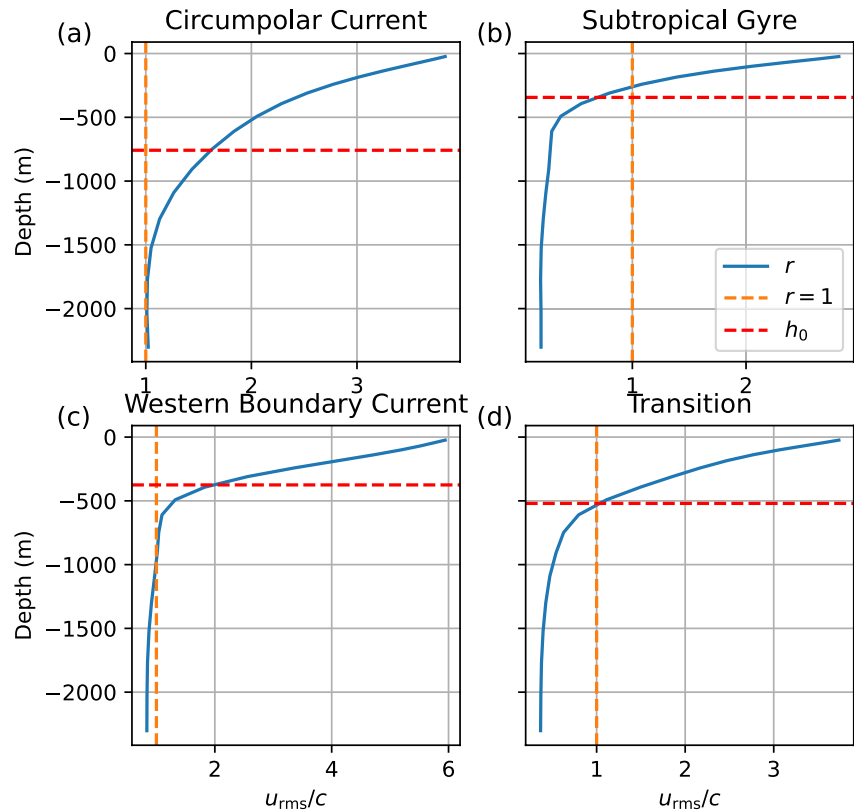


**Figure 10.** Vertical structure of the nonlinearity parameter, (8), (blue line) in the four regions shown in Figure 5. The orange dashed line gives  $r = 1$  and the red dashed line indicates the stratification scale depth,  $h_0$ .

Previous studies have found a transition from linear to nonlinear regime from tropics to midlatitude for the surface tracer mixing in the ocean, and the mixing in the nonlinear regime in midlatitudes is well-scaled by Prandtl MLT (Klocker & Abernathey, 2014; Klocker et al., 2016). This is consistent with our results in Figure 12a. This study further finds that such regime transition also happens with depth in the midlatitude ocean, and the mixing in linear regime in fact is better characterized by the Taylor regime. The Taylor regime also works for the mixing in the tropics shown in Figure 12b, which can complement previous studies to interpret the mixing in global ocean.

### 5.3. Mixing Length Scale

While the upper-ocean diffusivity is well-modeled by MLT with a depth-independent mixing length, the question of what determines this mixing length remains. The mixing length is commonly associated with the scale of the energy containing eddies (Ferrari & Nikurashin, 2010; Klocker & Abernathey, 2014; Larichev & Held, 1995; Stammer, 1998), though the method to estimate this energy containing scale differs. The most straightforward definition of the energy containing scale is simply the peak of the surface EKE spectrum (Larichev & Held, 1995), however resolving this peak accurately in wavenumber space requires large spatial windows that are problematic in the spatially inhomogeneous flow considered here. A more robust and local estimate of the energy containing scale is

$$L_0 = \sqrt{\frac{\overline{\eta''^2}}{|\nabla \eta''|^2}}, \quad (22)$$

where  $\eta''$  is the SSH anomaly from the 20-year mean (Ferrari & Nikurashin, 2010; Thompson & Young, 2006). In Figure 13 we compare the fitted mixing length in Figure 11 to  $L_0$  in the surface EKE spectrum. The inverse of both the fitted mixing length scale and  $L_0$  are close to the peak of the energy spectrum in all the four regions, consistent with the mixing length corresponding to the energy containing scale. (Note that the energy-containing

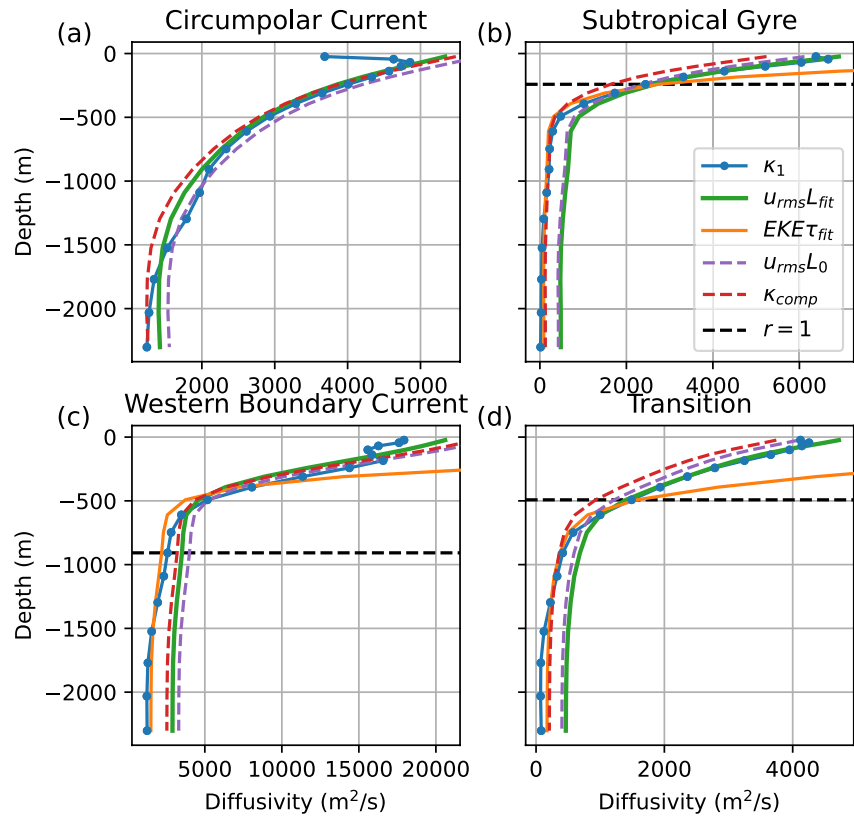


**Figure 11.** Scaling of the major diffusivity,  $\kappa_1$  (blue solid line with dots), at the same locations as in Figure 8. The depth where the nonlinearity parameter  $r = 1$  is indicated by black dashed lines in panels (b–d). Green lines show fits to the Prandtl regime (Equation 4) and orange lines show fits to the Taylor regime (Equation 6). The Prandtl and Taylor regime fits are only performed for depths where  $r > 1$  and  $r < 1$ , respectively, but the profiles are shown over the full depth. Taylor regime predictions (orange) significantly overestimate the diffusivity in the upper ocean and would extend far to the right of panels (b–d) if shown. Note that no Taylor regime fit is performed for panel (a). Purple dashed lines show Prandtl regime profiles with the mixing length estimated as the energy containing scale,  $L_0$ , instead of by fitting. Red dashed lines show composite profiles (Equation 25), with the mixing length as the energy containing scale,  $L_0$ , and mixing time scale as a uniform constant,  $\tau_0 = 24$  days—see Section 5.4.

scale corresponds to the radius of the energy-containing eddies. A single wavelength constitutes an eddy dipole so the radius of each eddy is one-fourth the wavelength, or approximately the inverse of the energy-containing wavenumber.) The horizontal distribution of  $L_0$  is given in figure C1b in Appendix C. The purple dashed line in Figure 11 shows the comparison between  $u_{rms} L_0$  and  $\kappa_1$ . The scaling with  $L_0$  matches the diffusivity in most of the regions, except that it slightly overestimates the mixing length in the western boundary current region.

#### 5.4. A Composite Profile for the Full-Depth Diffusivity

We have shown that  $\kappa_1$  follows a mixing length scaling (the Prandtl regime) when eddies are nonlinear ( $r > 1$ ) and a mixing time scaling (the Taylor regime) when the eddies are linear ( $r < 1$ ). These two regimes coexist in most regions, with the Prandtl regime holding in the upper ocean and the Taylor regime holding at depth. Here we propose a composite vertical profile that can smoothly transition from the Prandtl regime to the Taylor regime.

In the original form of SMLT (Ferrari & Nikurashin, 2010), the unsuppressed diffusivity,  $\kappa_u$ , is

$$\kappa_u(z) = \gamma^{-1}(z)EKE(z), \quad (23)$$

where  $\gamma$  is a decorrelation rate. Ferrari and Nikurashin (2010) estimate  $\gamma$  as the eddy turnover rate,  $u_{rms}/L_0$ , where  $L_0$  is the energy-containing scale (Equation 22). With this definition, (Equation 23) is equivalent to the



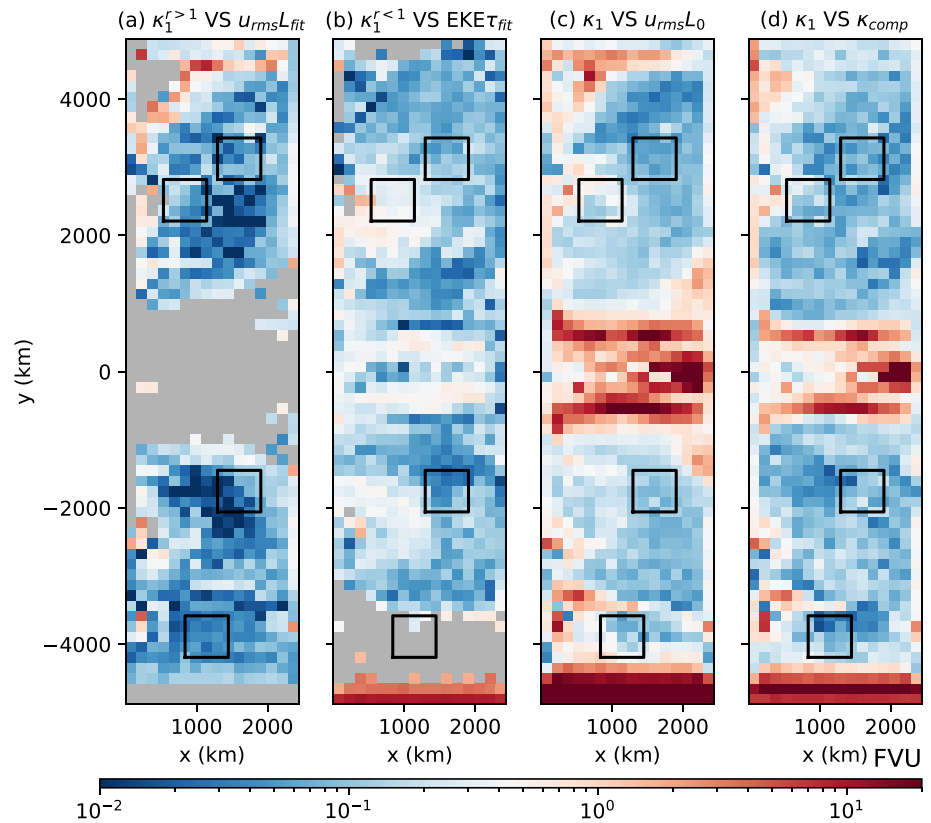


**Figure 12.** Fraction of variance unexplained (FVU) (20) for the comparison between the vertical profile of the major diffusivity,  $\kappa_1$ , and prediction by theories at each horizontal location. (a), (b) FVU for profiles of  $\kappa_1$  at depths where  $r > 1$  and  $r < 1$  compared to their fits to (a) the Prandtl regime (Equation 4) and (b) Taylor regime (Equation 6), respectively. Note that the regions where there are fewer than 4 levels for fitting are masked with gray color. (c), (d) FVU for the entire vertical profile of  $\kappa_1$  compared to (c)  $u_{rms}L_0$ , where  $L_0$  is the local energy-containing scale given by Equation 22, and (d) the composite scaling, given by Equation 25. Black boxes are the regions where the vertical structures of the diffusivities are analyzed in Figure 11. Note that negative diffusivities are excluded from the fitting and calculation of FVU.

MLT diffusivity (Equation 4). MLT assumes that the mixing is controlled by nonlinear eddy-eddy interactions; however, this is not the case in the deep ocean in the basin, where linear wave dynamics is more important.

To account for both the nonlinear and linear regimes, we assume that  $\gamma$  has contributions from both the eddy turnover rate,  $u_{rms}/L_0$ , and a depth-independent decay rate,  $\tau_0^{-1}$ , so

$$\gamma(z) = \frac{u_{rms}(z)}{L_0} + \frac{1}{\tau_0}. \quad (24)$$

The eddy turnover rate,  $u_{rms}/L_0$ , varies with depth and represents the contribution from nonlinear interactions (Ferrari & Nikurashin, 2010; Kong & Jansen, 2017). The decay time scale,  $\tau_0$ , is depth-independent and associated with a superposition of linear waves. This form of  $\gamma$  in Equation 24 is similar to that used by Klocker et al. (2012), who point out that the decorrelation time scale is set by the turnover time of turbulent eddies in upper ocean and by the time scale of linear waves in deep ocean. Adopting (Equation 24) in Equation 23, we obtain the composite formula

$$\kappa_{comp}(z) = \frac{u_{rms}(z)L_0}{1 + L_0/[u_{rms}(z)\tau_0]}. \quad (25)$$

The advantage of Equation 25 is that it smoothly transitions between the Prandtl and Taylor regimes. If  $u_{rms}/L_0$  dominates over  $\tau_0^{-1}$ , (Equation 25) reduces to the Prandtl regime expression, while if  $\tau_0^{-1}$  dominates, (Equation 25) reduces to the Taylor regime expression. Since  $u_{rms}$  decays rapidly with depth, the mixing regime described by

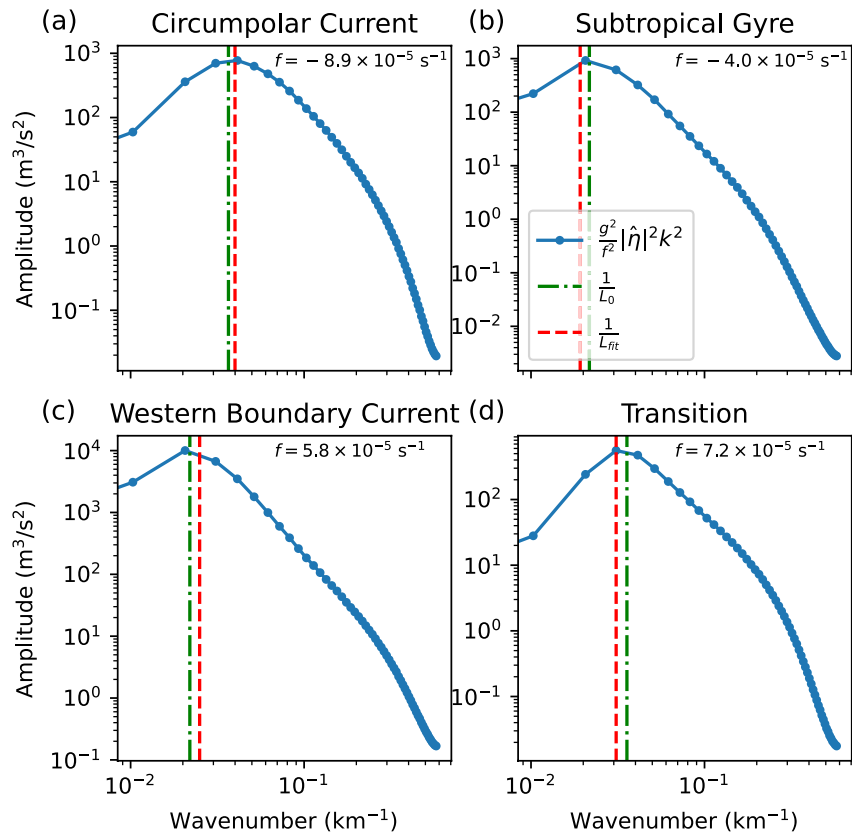


**Figure 13.** Surface geostrophic kinetic energy spectrum (blue solid line with dots) calculated from the instantaneous SSH fields over the four regions in Figure 5 and averaged over 20 years. The EKE spectrum is estimated as  $g^2 |\hat{\eta}|^2 k^2 / f^2$ , where  $\hat{\eta}$  is the Fourier transform of SSH,  $f$  is the spatial mean Coriolis parameter in each region (values given in the figure). The 2D spectrum is computed with tapering via a Tukey window, and then azimuthally integrated to obtain the 1D spectrum. The green dashed line indicates the inverse of the energy containing scale,  $L_0$ , estimated from Equation 22 at the center of the four regions, and red dashed line is the inverse of the fitted mixing length from Figure 11.

Equation 25 transitions from the Prandtl regime to the Taylor regime naturally with depth. An alternative way to achieve the regime transition is to use the nonlinearity parameter,  $r$ , in Equation 25 since the variation of  $r$  indicates the transition between nonlinear and linear regimes. However, we avoid the use of  $r$  since it is difficult to estimate in practice from the resolved fields of coarse-resolution models.

In Ferrari and Nikurashin (2010)'s derivation, the inverse of the decorrelation rate,  $1/\gamma$ , is equal to the time scale,  $\tau$ , in the suppression factor (18). However, if  $\tau = (u_{rms}/L_0 + 1/\tau_0)^{-1}$  is used in Equation 18, the relation  $\kappa_2 \approx \kappa_1 F_s$  no longer holds (not shown)—it is therefore better to treat  $\tau$  as a depth-independent time scale (i.e.,  $\tau = \tau_0$ ). This mismatch between  $\tau$  and  $1/\gamma$  was also noted by Klocker and Abernathey (2014), who attributed it to a shortcoming of the stochastic models of Ferrari and Nikurashin (2010) and Klocker et al. (2012). The fits of  $\kappa_2$  to  $\kappa_1 F_s$  in the circumpolar current, subtropical gyre and transition regions (c.f. Section 5.1 and Figure 8) give  $\tau_0$  as 22 days, 24 and 29 days, respectively, assuming the length scale,  $L$ , in Equation 18 is given by the local energy-containing scale,  $L_0$ . The fit in the western boundary current is not reliable because  $\kappa_2$  contains many negative values there. The time scales from the fits are close to the spin-down time scale due to the model's linear bottom drag, 25 days, which suggests  $\tau_0$  is related to frictional processes. We have no quantitative explanation for the spatial variation of  $\tau_0$ , so for simplicity we choose it to be a uniform constant. Following Groeskamp et al. (2020), we estimate it by doing an overall fit using diffusivity profiles from all three regions and find  $\tau_0 \approx 24$  days—which is again close to the frictional spin-down time.

The composite profile,  $\kappa_{comp}$ , with  $\tau_0 = 24$  days is compared to the vertical structure of the major diffusivity,  $\kappa_1$ , in Figure 11 (red dashed line). The composite profile captures the variation of full-depth diffusivity better than MLT (purple dashed line) in the four regions. The composite profile slightly underestimates the diffusivity in the upper ocean in the subtropical gyre and transition regions compared with MLT, but its overall comparison with  $\kappa_1$

is better than MLT. The relative performance of the composite profile and MLT are assessed using the FVU (20) and shown in Figures 12c & 12d. The composite profile prediction of  $\kappa_1$  performs better than MLT, especially in the subtropical gyres. The success of the composite profile verifies our assumption that both the nonlinear eddy-eddy interaction and decay of linear waves contribute to the mixing. The composite profile does not work well in the eastern tropics or the boundary between tropics and subtropics. The fits show that the mixing time scale,  $\tau_0$ , is smaller than 24 days in those regions, which suggests that a better physical estimate for  $\tau_0$  is necessary to further capture the variation of diffusivity in the tropics.

The cross-stream diffusivity,  $\kappa_2$ , is also estimated by multiplying  $\kappa_{\text{comp}}$  by the suppression factor  $F_s^0$ ,

$$F_s^0(z) = \frac{1}{1 + \frac{\tau_0^2}{L_0^2} [c_w - \bar{u}(z)]^2}, \quad (26)$$

where  $c_w$  and  $\bar{u}$  are taken the same as those in Section 5.1. The estimate of  $\kappa_{\text{comp}} F_s^0$  is shown by the red dashed line in Figure 8. The estimate with SMLT (i.e.,  $u_{\text{rms}} L_0 F_s^0$ ) is also shown in Figure 8 (purple dashed line) for comparison. SMLT only captures the vertical structure of  $\kappa_2$  well in the circumpolar current region, while the suppressed composite profile,  $\kappa_{\text{comp}} F_s^0$ , works well in both the circumpolar current and the gyres. The poor estimate in the western boundary current might be due to the presence of negative values for the minor diffusivity (Figure 3), which could potentially lead to large uncertainties in the profile. The FVU for the comparisons between the vertical profile of  $\kappa_2$  and the predictions by SMLT and  $\kappa_{\text{comp}} F_s^0$  are given in Figure 9b and 9c, respectively. The composite profile improves the prediction of  $\kappa_2$  compared with the SMLT in the subtropical and subpolar regions. The suppressed composite profile,  $\kappa_{\text{comp}} F_s^0$ , is applicable to broader ocean regimes than SMLT, which makes it a promising estimate for the cross-stream diffusivity from ocean observations.

The FVU for both the suppressed composite profile and SMLT are large in many regions in the circumpolar current. The error is mostly due to the underestimates of the diffusivity in the deep circumpolar current, where  $\kappa_2$  decreases with depth more slowly than the predictions as shown in Figure 8a, but its qualitative features are still captured. The mixing tends to become isotropic in the deep circumpolar current as shown in Figure 5a and Figure 6a, and the mean flow suppression appears to be weaker than the prediction by Equation 26. Wolfram and Ringler (2017) also found that the cross-stream diffusivity decreases with depth slower than the prediction by SMLT in the deep ocean. They argued that this issue might be fixed by making  $L_0$  and  $\tau_0$  in Equation 26 vary with depth, but the estimation of the vertical structure of  $L_0$  and  $\tau_0$  requires additional physical understanding.

## 6. Conclusions

This study investigates the vertical structure of the isopycnal tracer diffusivity in an idealized basin configuration of the MITgcm, which contains multiple gyres, boundary currents, and a zonally reentrant channel flow analogous to the Antarctic Circumpolar Current. Multiple tracers are advected to solve for the 3D diffusivity tensor based on the tracer-inversion method of S. D. Bachman et al. (2015). As shown in Appendix B, the reconstruction of eddy tracer fluxes from the diffusivity tensor is excellent, even for active tracers not used to diagnose the diffusivity tensor. The diffusivity tensor is additionally insensitive to the details of the tracers used in the pseudoinversion as long as a sufficient number of linearly independent tracers are used. These results indicate that the diffusivity tensor so diagnosed is generic and capable of representing the eddy flux of an arbitrary tracer.

Recent studies reporting that the diffusivity tensor is highly sensitive to the tracers used to estimate it (e.g., Haigh et al., 2021; Kamenkovich et al., 2021; Sun et al., 2021) have used the minimum number of tracers required to determine the diffusivity tensor (e.g., two tracers for a  $2 \times 2$  tensor). Such inversion methods rely on the assumption that arbitrary pairs (or triplets for a  $3 \times 3$  tensor) of tracers will remain linearly independent at all spatial points in the simulation domain. This is unlikely to be true in practice, which can make the resulting inversion extremely ill-conditioned. In contrast, using many tracers allows the pseudoinversion process to automatically remove linearly dependent tracer combinations so that the inversion remains well-conditioned and robust. Note that these statements apply to the representation of the time mean eddy flux on coarsened grids—the instantaneous tracer flux on the original grid may not be represented in detail. Further, since the diagnosed diffusivities are effectively time-invariant, using them to represent the fluxes of active tracers will lead to an eventual accumulation of errors due to the lack of feedback between the diffusivities and the fluxes. We therefore acknowledge the possibility that

the diffusivity tensor necessary to represent instantaneous fluxes of (possibly active) tracers may indeed depend on the tracers in question and suggest that the diffusivities obtained from pseudoinversion are more suited for diagnostic rather than prognostic studies.

The first two eigenvectors of the symmetrized diffusivity tensor are approximately aligned with buoyancy surfaces, so the associated eigenvalues represent isopycnal diffusivities. The isopycnal diffusivities are anisotropic, with the diffusivity along the mean flow generally several times larger than the diffusivity across the mean flow. The cross-stream diffusivity tends to have a subsurface maximum and can be reconstructed from the vertical profile of along-stream diffusivity after accounting for mixing suppression by eddy propagation relative to the mean flow (K. S. Smith & Marshall, 2009; Ferrari & Nikurashin, 2010; Klocker et al., 2012). This suggests that the anisotropy of mixing is primarily due to the mean flow suppression of the cross-stream diffusivity, rather than shear dispersion.

The vertical structure of the along-stream diffusivity is well-captured by Prandtl mixing length theory with a depth-independent mixing length where the nonlinearity parameter  $r > 1$ ; this is in the circumpolar current and above the thermocline in the basin regions. The mixing length is well-approximated by the energy containing scale estimated from the SSH anomaly, which is straightforward to diagnose based on Equation 22 using SSH from satellite altimetry. No nondimensional mixing efficiency needs to be specified in this scaling, which is an advantage over previous studies (e.g., Groeskamp et al., 2020; Klocker & Abernathey, 2014). The success of Prandtl scaling in the upper ocean in this model provides a rationalization for studies which apply mixing length theory to infer the vertical structure of diffusivity assuming that the mixing length is depth-independent (Bates et al., 2014; Groeskamp et al., 2020).

The nonlinearity parameter  $r < 1$  below the thermocline in the basin, so a depth-independent mixing length does not apply. Indeed, using the upper-ocean mixing length can overestimate the deep diffusivity in the gyres by nearly an order of magnitude. Although the diffusivity is generally small at depth, excessively large diffusivities may still significantly impact deep watermasses and the mean state over long simulations since the mean flow is also very weak at depth. The along-stream diffusivity in the linear regime ( $r < 1$ ) in the deep ocean is well-represented by the Taylor regime (i.e., the EKE times a depth-independent mixing time scale). This dependence of mixing regime on nonlinearity is consistent with the arguments of Klocker and Abernathey (2014) and Klocker et al. (2016), who find that mixing length theory applies to surface mixing in the extratropics where the flow is nonlinear but fails in the tropics where the flow is dominated by linear waves. This study shows that a similar transition can also occur in the vertical near the base of thermocline in the midlatitudes. Mixing length theory only characterizes the full-depth diffusivity well in the circumpolar current, where the flow is nonlinear ( $r > 1$ ) over the full depth.

To account for the transition between nonlinear and linear mixing regimes, we propose a composite scaling profile in which the decorrelation rate has contributions from both the eddy turnover rate and a depth-independent decay rate. This profile reduces to the Prandtl regime where the eddy turnover rate dominates and to the Taylor regime where the decay rate dominates, with a smooth transition between them. The composite profile captures the vertical structure of the along-stream diffusivity better than either the Prandtl or Taylor regime alone. The cross-stream diffusivity is also well-characterized by the composite profile multiplied by a suppression factor, (Equation 26), which accounts for the suppression of mixing by the mean flow (Ferrari & Nikurashin, 2010; Klocker et al., 2012). The composite profile has the advantage of capturing both the nonlinear and linear regimes and should be useful in estimates or parameterizations of the full-depth isopycnal mixing in a broad range of ocean regimes.

The model used in this study does not have bottom topography, which likely impacts the vertical structure of EKE and the tracer diffusivities. The presence of bottom topography can reduce the EKE near the bottom and make it more surface intensified (de La Lama et al., 2016; LaCasce, 2017). The topographic waves will also likely play an important role in the mixing in the deep ocean (Hallberg, 1997; Rhines, 1970). These possible changes might make eddies become more nonlinear in the upper ocean due to a greater surface-intensification of EKE and make linear dynamics more significant in the deep ocean due to the presence of topographic waves. Topography can also change the direction of the mean flow and PV gradient, especially in the circumpolar current region, where the mean flow is strong near the bottom. This can change the major and minor directions of isopycnal mixing (S. D. Bachman, 2021) and even lead to the breakdown of mixing suppression due to the presence of non-parallel jets (Naveira Garabato et al., 2011; Thompson, 2010). Finally, topography can alter the mixing length (Wei & Wang, 2021) and eddy phase speed (LaCasce & Groeskamp, 2020; Tailleux & McWilliams, 2001). Application of the results of this study to simulations with bottom topography will be pursued in the future work.

The scaling proposed by this study is not a full closure theory, since it still requires the vertical profile of the eddy kinetic energy and the energy containing scale from the SSH anomaly. Tests of the existing closure theories for the mixing length (e.g., Visbeck et al., 1997; Eden & Greatbatch, 2008; Thompson & Young, 2006; Jansen et al., 2015; Gallet & Ferrari, 2020, 2021) and vertical mode theory of the eddy kinetic energy (e.g., Wunsch, 1997; Lapeyre & Klein, 2006; LaCasce & Mahadevan, 2006; K. S.; Smith & Vanneste, 2013; LaCasce, 2017; Groeskamp et al., 2020) is beyond of the scope of this study and will be studied in a forthcoming paper. In addition, the mean flow suppression theory used in this study is based on a single energy containing wavenumber as in Ferrari and Nikurashin (2010). However, studies have suggested that better estimate of the diffusivity can be obtained using whole energy spectrum (Chen et al., 2015; Kong & Jansen, 2017). Thus for a full closure, we will also need a prediction for the EKE spectrum. A closure theory including all these factors would serve as a solid parameterization of the isopycnal mixing in the ocean component of coarse-resolution climate models.

### Appendix A: Identification and Tracking of Coherent Mesoscale Eddies

Coherent mesoscale eddies are identified and tracked using SSH snapshots in three-day intervals from the model, using the same algorithm as Chelton et al. (2011). This method is provided as an optional tracking method in the eddy tracking package described by Mason et al. (2014). Coherent eddies are identified as the SSH extrema and tracked by connecting each eddy to the proximal eddies in successive time frames, where the eddies amplitude and radius are required to be 0.4–2.5 times those of the corresponding eddies in the last time frame. Only the eddies that last longer than 30 days are considered. The propagation velocity of coherent eddies at time step  $m$  is estimated as the centered difference from locations of the eddy centroids at the time steps  $m - 1$  and  $m + 1$ . See Chelton et al. (2011) and Mason et al. (2014) for more detail.

### Appendix B: Evaluation of the Reliability and Robustness of the Diffusivity Tensor

To test the effectiveness of pseudoinversion method, the flux of each of the 27 tracers and the heat flux are reconstructed using the diffusivity tensor,  $\mathbf{K}$ . Note that the heat flux is not used in the tracer inversion in Equation 14, so it can be used as an independent test for the effectiveness of  $\mathbf{K}$ . Following S. D. Bachman et al. (2020) the relative error of reconstructed tracer flux is estimated as

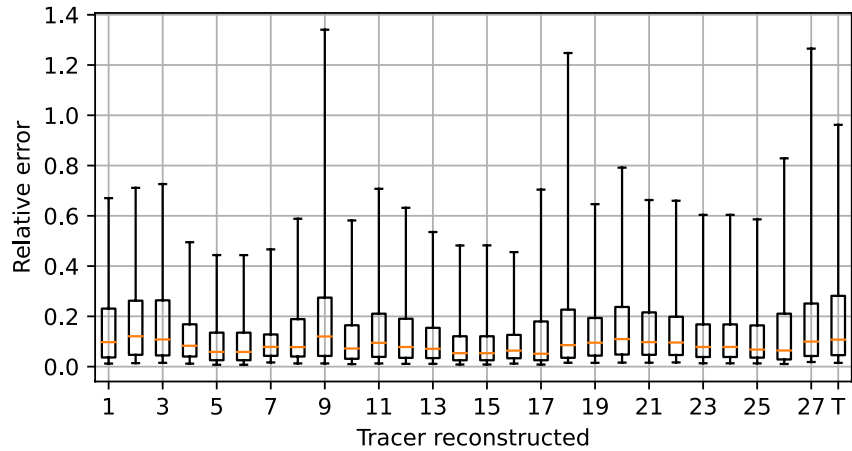
$$\epsilon = \frac{\|\mathbf{u}'C' + \mathbf{K}\nabla\bar{C}\|}{\|\mathbf{u}'C'\|}, \quad (\text{B1})$$

where  $C$  is one of the 27 tracers or the temperature and  $\|\cdot\|$  is the vector norm. The relative error of the tracer flux reconstruction is estimated at each coarsened grid point and vertical level and the distribution is shown in Figure B1. The relative error is generally small at the majority of the grid points, with a median smaller than 0.2, so the diffusivity tensor captures most the characteristics of eddy tracer transport. Tracers  $C_9$ ,  $C_{18}$  and  $C_{27}$  have the largest relative error, because their initial vertical gradient is close to zero at some levels, which leads to very small tracer flux at those levels and make the relative error appear very large. With the exception of these tracers, the reconstruction is not very different for tracers with different initial distributions, indicating that the diffusivity tensor is generic and capable of representing the eddy flux of an arbitrary tracer.

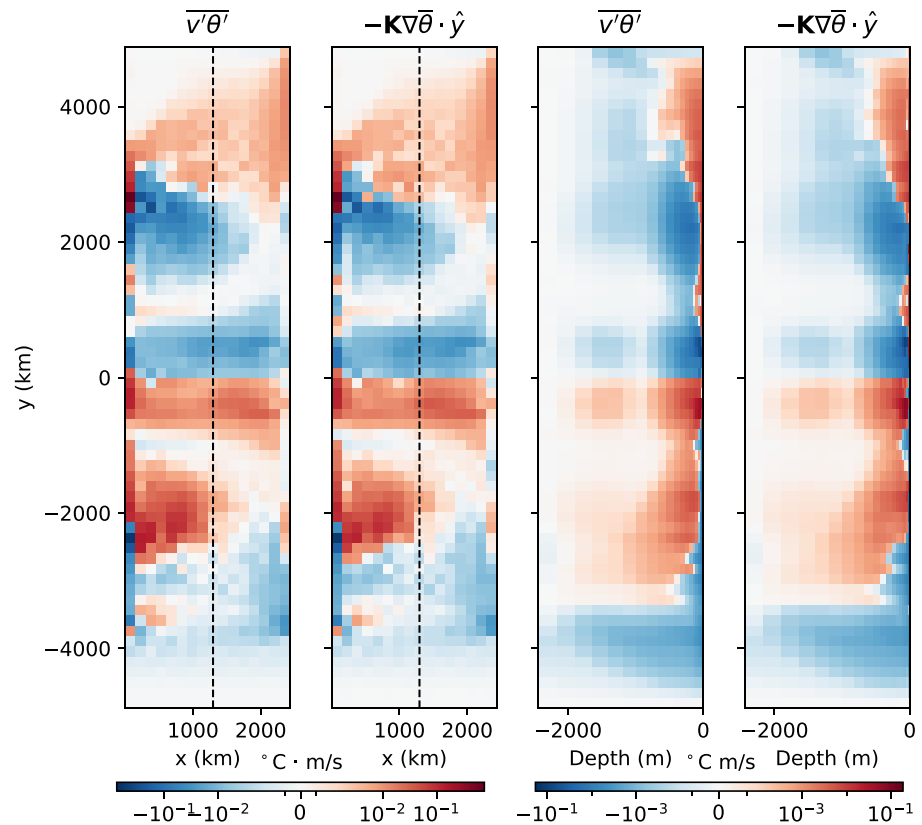
We tried to use fewer tracers (e.g., only using tracers 1–9) in the inversion, and the relative error is not very different from the inversion using all 27 tracers (not shown), which suggests that 9 tracers with distinct initial distributions are likely sufficient to diagnose the diffusivity tensor. In the rest of the paper we simply used the diffusivity tensor  $\mathbf{K}$  diagnosed using all the 27 tracers.

Figure B2 compares the meridional heat flux reconstructed by the diffusivity tensor with the diagnosed heat flux at 138 m depth (same depth as Figure 3) and a meridionally oriented vertical section, indicated by the black dashed line in Figure B2a and B2b. The reconstructed heat flux looks very similar as the diagnosed heat flux, meaning that the diffusivity tensor excellently reconstructs the meridional heat flux of the model. Note that the heat flux and temperature gradient are not used in the tracer inversion (14), so heat flux is independent from the calculation of the diffusivity tensor. The accurate reconstruction of the meridional heat flux thus supports the assumption behind (14) that the diffusivity tensor is independent of the particular tracers used in the inversion.





**Figure B1.** Box and whisker plot of the relative error of the tracer flux reconstruction, calculated by (B1) at all coarsened grid points and weighted by volume. The labels on the abscissa indicate the tracer whose flux is reconstructed (the number  $i$  indicates  $C_i$  and  $T$  indicates temperature). The orange line gives the median value and the box extends from the first to the third quartile of the error distribution. The upper and lower whiskers indicate the 5 and 95 percentiles.



**Figure B2.** Meridional heat flux (a), (c) diagnosed from the model and (b), (d) reconstructed by the diffusivity tensor. (a) and (b) show the horizontal distribution of the heat flux at 138 m depth. (c) and (d) show the vertical distribution of heat flux at a meridional section indicated by the black dashed line in (a) and (b).

### Appendix C: Mixing Length and Time Scales

Figure C1a and C1c give the distribution of the mixing length and time scales from the fits in Figure 12a and 12b, respectively. The mixing length is typically tens of kilometers and decreases from the subtropics to the high latitudes. The ratio of the mixing length to the local Rossby deformation radius increases from around 1 in the subtropics ( $y \sim 1,000\text{--}2,000$  km) to around 2.5 in the high latitudes ( $y \sim 4,000$  km), which is consistent with the observationally based results of Klocker and Abernathy (2014). The mixing length is close to the energy containing scale,  $L_0$ , (Figure C1b) in most extra-tropical regions. The fitted mixing time scale is smallest in the tropics and varies little in the gyres, where it is close to the spin-down time scale due to the model's linear bottom drag, 25 days.

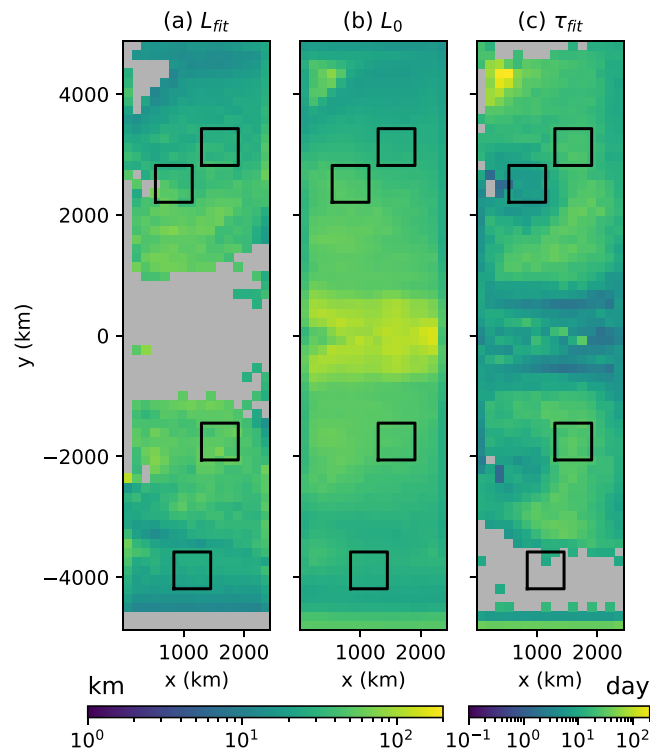


**Figure C1.** Distribution of the (a) fitted mixing length in Figure 12a and (b) the energy containing scale,  $L_0$ , estimated by Equation 22 and (c) fitted mixing time scale in Figure 12b. Black boxes are as in Figure 12.

#### Acknowledgments

This work is supported by the National Science Foundation (NSF) through Award OCE-2048826. Computing resources were provided by the high-performance SeaWulf computing system supported by Stony Brook Research Computing and Cyber Infrastructure and the Institute for Advanced Computational Science at Stony Brook University, which is itself supported by NSF. We are grateful to Shafer Smith for insightful comments and sharing an unpublished manuscript on the use of multiple tracers by Dhruv Balwada, Shafer Smith, and Ryan Abernathy. We also thank Scott Bachman and Yan Wang for helpful discussions on the tracer inversion method and analysis. We thank three anonymous reviewers and the editor Stephen Griffies for their insightful comments, which helped to significantly improve the manuscript.

#### Data Availability Statement

Model configuration, analysis scripts, data files used for this study are available at <https://doi.org/10.5281/zenodo.6466362>.

#### References

- Abernathy, R., Ferreira, D., & Klocker, A. (2013). Diagnostics of isopycnal mixing in a circumpolar channel. *Ocean Modelling*, 72, 1–16. <https://doi.org/10.1016/j.ocemod.2013.07.004>
- Abernathy, R., Marshall, J., Mazloff, M., & Shuckburgh, E. (2010). Enhancement of mesoscale eddy stirring at steering levels in the Southern Ocean. *Journal of Physical Oceanography*, 40(1), 170–184. <https://doi.org/10.1175/2009jpo4201.1>
- Abernathy, R. P., & Marshall, J. (2013). Global surface eddy diffusivities derived from satellite altimetry. *Journal of Geophysical Research: Oceans*, 118(2), 901–916. <https://doi.org/10.1002/jgrc.20066>
- Adcroft, A., Anderson, W., Balaji, V., Blanton, C., Bushuk, M., Dufour, C. O., et al. (2019). The GFDL global ocean and sea ice model OM4.0: Model description and simulation features. *Journal of Advances in Modeling Earth Systems*, 11(10), 3167–3211. <https://doi.org/10.1029/2019ms001726>

- Bachman, S., & Fox-Kemper, B. (2013). Eddy parameterization challenge suite I: Eady spindown. *Ocean Modelling*, *64*, 12–28. <https://doi.org/10.1016/j.ocemod.2012.12.003>
- Bachman, S. D. (2021). An Eulerian scheme for identifying fronts and vortices in quasi-balanced flows. *Journal of Physical Oceanography*. <https://doi.org/10.1175/jpo-d-21-0037.1>
- Bachman, S. D., Fox-Kemper, B., & Bryan, F. O. (2015). A tracer-based inversion method for diagnosing eddy-induced diffusivity and advection. *Ocean Modelling*, *86*, 1–14. <https://doi.org/10.1016/j.ocemod.2014.11.006>
- Bachman, S. D., Fox-Kemper, B., & Bryan, F. O. (2020). A diagnosis of anisotropic eddy diffusion from a high-resolution global ocean model. *Journal of Advances in Modeling Earth Systems*, *12*(2), e2019MS001904. <https://doi.org/10.1029/2019ms001904>
- Bates, M., Tulloch, R., Marshall, J., & Ferrari, R. (2014). Rationalizing the spatial distribution of mesoscale eddy diffusivity in terms of mixing length theory. *Journal of Physical Oceanography*, *44*(6), 1523–1540. <https://doi.org/10.1175/jpo-d-13-0130.1>
- Campin, J.-M., Heimbach, P., Losch, M., Forget, G., Hill, E., Adcroft, A., et al. (2020). MITgcm. Zenodo. <https://doi.org/10.5281/zenodo.3967889>
- Cessi, P. (2008). An energy-constrained parameterization of eddy buoyancy flux. *Journal of Physical Oceanography*, *38*(8), 1807–1819. <https://doi.org/10.1175/2007jpo3812.1>
- Cessi, P., & Wolfe, C. L. (2009). Eddy-driven buoyancy gradients on eastern boundaries and their role in the thermocline. *Journal of Physical Oceanography*, *39*(7), 1595–1614. <https://doi.org/10.1175/2009jpo4063.1>
- Cessi, P., Wolfe, C. L., & Ludka, B. C. (2010). Eastern-boundary contribution to the residual and meridional overturning circulations. *Journal of Physical Oceanography*, *40*(9), 2075–2090. <https://doi.org/10.1175/2010JPO4426.1>
- Chapman, C., & Sallée, J.-B. (2017). Isopycnal mixing suppression by the Antarctic Circumpolar Current and the Southern Ocean meridional overturning circulation. *Journal of Physical Oceanography*, *47*(8), 2023–2045. <https://doi.org/10.1175/jpo-d-16-0263.1>
- Charney, J. G. (1947). The dynamics of long waves in a baroclinic westerly current. *Journal of Meteorology*, *4*(5), 136–162. [https://doi.org/10.1175/1520-0469\(1947\)004<0136:tdolwi>2.0.co;2](https://doi.org/10.1175/1520-0469(1947)004<0136:tdolwi>2.0.co;2)
- Chelton, D. B., Schlax, M. G., & Samelson, R. M. (2011). Global observations of nonlinear mesoscale eddies. *Progress in Oceanography*, *91*(2), 167–216. <https://doi.org/10.1016/j.pocean.2011.01.002>
- Chen, R., Gille, S. T., McClean, J. L., Flierl, G. R., & Griesel, A. (2015). A multiwavenumber theory for eddy diffusivities and its application to the southeast Pacific (DIMES) region. *Journal of Physical Oceanography*, *45*(7), 1877–1896. <https://doi.org/10.1175/jpo-d-14-0229.1>
- Chen, R., McClean, J. L., Gille, S. T., & Griesel, A. (2014). Isopycnal eddy diffusivities and critical layers in the Kuroshio Extension from an eddying ocean model. *Journal of Physical Oceanography*, *44*(8), 2191–2211. <https://doi.org/10.1175/jpo-d-13-0258.1>
- Chen, R., & Waterman, S. (2017). Mixing nonlocality and mixing anisotropy in an idealized western boundary current jet. *Journal of Physical Oceanography*, *47*(12), 3015–3036. <https://doi.org/10.1175/jpo-d-17-0011.1>
- Cole, S. T., Wortham, C., Kunze, E., & Owens, W. B. (2015). Eddy stirring and horizontal diffusivity from Argo float observations: Geographic and depth variability. *Geophysical Research Letters*, *42*(10), 3989–3997. <https://doi.org/10.1002/2015gl063827>
- Daru, V., & Tenaud, C. (2004). High order one-step monotonicity-preserving schemes for unsteady compressible flow calculations. *Journal of Computational Physics*, *193*(2), 563–594. <https://doi.org/10.1016/j.jcp.2003.08.023>
- de La Lama, M. S., LaCasce, J., & Fuhr, H. K. (2016). The vertical structure of ocean eddies. *Dynamics and Statistics of the Climate System*, *1*(1).
- Eden, C., & Greatbatch, R. J. (2008). Towards a mesoscale eddy closure. *Ocean Modelling*, *20*(3), 223–239. <https://doi.org/10.1016/j.ocemod.2007.09.002>
- Ferrari, R., & Nikurashin, M. (2010). Suppression of eddy diffusivity across jets in the Southern Ocean. *Journal of Physical Oceanography*, *40*(7), 1501–1519. <https://doi.org/10.1175/2010jpo4278.1>
- Ferrari, R., & Wunsch, C. (2009). Ocean circulation kinetic energy: Reservoirs, sources, and sinks. *Annual Review of Fluid Mechanics*, *41*(1), 253–282. <https://doi.org/10.1146/annurev.fluid.40.111406.102139>
- Fox-Kemper, B., Lumpkin, R., & Bryan, F. (2013). Lateral transport in the ocean interior. In G. Siedler, S. M. Griffies, J. Gould, & J. A. Church (Eds.), *Ocean circulation and climate* (Vol. 103, pp. 185–209). Academic Press. <https://doi.org/10.1016/B978-0-12-391851-2.00008-8>
- Gallet, B., & Ferrari, R. (2020). The vortex gas scaling regime of baroclinic turbulence. *Proceedings of the National Academy of Sciences of the United States of America*, *117*(9), 4491–4497. <https://doi.org/10.1073/pnas.1916272117>
- Gallet, B., & Ferrari, R. (2021). A quantitative scaling theory for meridional heat transport in planetary atmospheres and oceans. *AGU Advances*, *2*(3), e2020AV000362. <https://doi.org/10.1029/2020av000362>
- Gent, P. R., & McWilliams, J. C. (1990). Isopycnal mixing in ocean circulation models. *Journal of Physical Oceanography*, *20*(1), 150–155. [https://doi.org/10.1175/1520-0485\(1990\)020<0150:imiocm>2.0.co;2](https://doi.org/10.1175/1520-0485(1990)020<0150:imiocm>2.0.co;2)
- Gent, P. R., Willebrand, J., McDougall, T. J., & McWilliams, J. C. (1995). Parameterizing eddy-induced tracer transports in ocean circulation models. *Journal of Physical Oceanography*, *25*(4), 463–474. [https://doi.org/10.1175/1520-0485\(1995\)025<0463:peitti>2.0.co;2](https://doi.org/10.1175/1520-0485(1995)025<0463:peitti>2.0.co;2)
- Gnanadesikan, A., Pradal, M.-A., & Abernathy, R. (2015). Isopycnal mixing by mesoscale eddies significantly impacts oceanic anthropogenic carbon uptake. *Geophysical Research Letters*, *42*(11), 4249–4255. <https://doi.org/10.1002/2015gl064100>
- Green, J. S. A. (1960). A problem in baroclinic stability. *Quarterly Journal of the Royal Meteorological Society*, *86*(368), 237–251. <https://doi.org/10.1002/qj.49708636813>
- Griesel, A., Eden, C., Koopmann, N., & Yulaeva, E. (2015). Comparing isopycnal eddy diffusivities in the Southern Ocean with predictions from linear theory. *Ocean Modelling*, *94*, 33–45. <https://doi.org/10.1016/j.ocemod.2015.08.001>
- Griesel, A., McClean, J., Gille, S., Sprintall, J., & Eden, C. (2014). Eulerian and Lagrangian isopycnal eddy diffusivities in the Southern Ocean of an eddying model. *Journal of Physical Oceanography*, *44*(2), 644–661. <https://doi.org/10.1175/jpo-d-13-039.1>
- Griffies, S. M. (1998). The Gent–McWilliams skew flux. *Journal of Physical Oceanography*, *28*(5), 831–841. [https://doi.org/10.1175/1520-0485\(1998\)028<0831:tgmfs>2.0.co;2](https://doi.org/10.1175/1520-0485(1998)028<0831:tgmfs>2.0.co;2)
- Groeskamp, S., LaCasce, J. H., McDougall, T. J., & Rogé, M. (2020). Full-depth global estimates of ocean mesoscale eddy mixing from observations and theory. *Geophysical Research Letters*, *47*(18), e2020GL089425. <https://doi.org/10.1029/2020gl089425>
- Groeskamp, S., Sloyan, B. M., Zika, J. D., & McDougall, T. J. (2017). Mixing inferred from an ocean climatology and surface fluxes. *Journal of Physical Oceanography*, *47*(3), 667–687. <https://doi.org/10.1175/jpo-d-16-0125.1>
- Haigh, M., Sun, L., McWilliams, J. C., & Berloff, P. (2021). On eddy transport in the ocean. part I: The diffusion tensor. *Ocean Modelling*, *164*, 101831. <https://doi.org/10.1016/j.ocemod.2021.101831>
- Hallberg, R. (1997). Localized coupling between surface and bottom-intensified flow over topography. *Journal of Physical Oceanography*, *27*(6), 977–998. [https://doi.org/10.1175/1520-0485\(1997\)027<0977:lcbasb>2.0.co;2](https://doi.org/10.1175/1520-0485(1997)027<0977:lcbasb>2.0.co;2)
- Hallberg, R., & Gnanadesikan, A. (2006). The role of eddies in determining the structure and response of the wind-driven Southern Hemisphere overturning: Results from the modeling eddies in the Southern Ocean (MESO) project. *Journal of Physical Oceanography*, *36*(12), 2232–2252. <https://doi.org/10.1175/jpo2980.1>

- Jansen, M. F., Adcroft, A. J., Hallberg, R., & Held, I. M. (2015). Parameterization of eddy fluxes based on a mesoscale energy budget. *Ocean Modelling*, 92, 28–41. <https://doi.org/10.1016/j.ocemod.2015.05.007>
- Jones, C., & Abernathy, R. P. (2019). Isopycnal mixing controls deep ocean ventilation. *Geophysical Research Letters*, 46(22), 13144–13151. <https://doi.org/10.1029/2019gl085208>
- Kamenkovich, I., Berloff, P., Haigh, M., Sun, L., & Lu, Y. (2021). Complexity of mesoscale eddy diffusivity in the ocean. *Geophysical Research Letters*, 48(5), e2020GL091719. <https://doi.org/10.1029/2020gl091719>
- Kamenkovich, I., Rypina, I. I., & Berloff, P. (2015). Properties and origins of the anisotropic eddy-induced transport in the North Atlantic. *Journal of Physical Oceanography*, 45(3), 778–791. <https://doi.org/10.1175/jpo-d-14-0164.1>
- Killworth, P. D. (1997). On the parameterization of eddy transfer Part I. Theory. *Journal of Marine Research*, 55(6), 1171–1197. <https://doi.org/10.1357/0022240973224102>
- Klocker, A., & Abernathy, R. (2014). Global patterns of mesoscale eddy properties and diffusivities. *Journal of Physical Oceanography*, 44(3), 1030–1046. <https://doi.org/10.1175/jpo-d-13-0159.1>
- Klocker, A., Ferrari, R., & LaCasce, J. H. (2012). Estimating suppression of eddy mixing by mean flows. *Journal of Physical Oceanography*, 42(9), 1566–1576. <https://doi.org/10.1175/jpo-d-11-0205.1>
- Klocker, A., & Marshall, D. P. (2014). Advection of baroclinic eddies by depth mean flow. *Geophysical Research Letters*, 41(10), 3517–3521. <https://doi.org/10.1002/2014gl060001>
- Klocker, A., Marshall, D. P., Keating, S. R., & Read, P. L. (2016). A regime diagram for ocean geostrophic turbulence. *Quarterly Journal of the Royal Meteorological Society*, 142(699), 2411–2417. <https://doi.org/10.1002/qj.2833>
- Kong, H., & Jansen, M. (2017). The eddy diffusivity in barotropic  $\beta$ -plane turbulence. *Fluid*, 2(4), 54. <https://doi.org/10.3390/fluids2040054>
- LaCasce, J., & Groeskamp, S. (2020). Baroclinic modes over rough bathymetry and the surface deformation radius. *Journal of Physical Oceanography*, 50(10), 1–40. <https://doi.org/10.1175/jpo-d-20-0055.1>
- LaCasce, J. H. (2017). The prevalence of oceanic surface modes. *Geophysical Research Letters*, 44(21), 11–097. <https://doi.org/10.1002/2017gl075430>
- LaCasce, J. H., & Mahadevan, A. (2006). Estimating subsurface horizontal and vertical velocities from sea-surface temperature. *Journal of Marine Research*, 64(5), 695–721. <https://doi.org/10.1357/002224006779367267>
- Lapeyre, G., & Klein, P. (2006). Dynamics of the upper oceanic layers in terms of surface quasigeostrophy theory. *Journal of Physical Oceanography*, 36(2), 165–176. <https://doi.org/10.1175/jpo2840.1>
- Larichev, V. D., & Held, I. M. (1995). Eddy amplitudes and fluxes in a homogeneous model of fully developed baroclinic instability. *Journal of Physical Oceanography*, 25(10), 2285–2297. [https://doi.org/10.1175/1520-0485\(1995\)025<2285:eaafia>2.0.co;2](https://doi.org/10.1175/1520-0485(1995)025<2285:eaafia>2.0.co;2)
- Ledwell, J. R., Watson, A. J., & Law, C. S. (1998). Mixing of a tracer in the pycnocline. *Journal of Geophysical Research*, 103(C10), 21499–21529. <https://doi.org/10.1029/98jc01738>
- Marshall, D. P., & Adcroft, A. J. (2010). Parameterization of ocean eddies: Potential vorticity mixing, energetics and Arnold's first stability theorem. *Ocean Modelling*, 32(3–4), 188–204. <https://doi.org/10.1016/j.ocemod.2010.02.001>
- Marshall, D. P., Maddison, J. R., & Berloff, P. S. (2012). A framework for parameterizing eddy potential vorticity fluxes. *Journal of Physical Oceanography*, 42(4), 539–557. <https://doi.org/10.1175/jpo-d-11-048.1>
- Marshall, J., Adcroft, A., Hill, C., Perelman, L., & Heisey, C. (1997). A finite-volume, incompressible Navier Stokes model for studies of the ocean on parallel computers. *Journal of Geophysical Research*, 102(C3), 5753–5766. <https://doi.org/10.1029/96JC02775>
- Marshall, J., Hill, C., Perelman, L., & Adcroft, A. (1997). Hydrostatic, quasi-hydrostatic, and nonhydrostatic ocean modeling. *Journal of Geophysical Research*, 102(C3), 5733–5752. <https://doi.org/10.1029/96JC02776>
- Marshall, J., & Radko, T. (2003). Residual-mean solutions for the Antarctic Circumpolar Current and its associated overturning circulation. *Journal of Physical Oceanography*, 33(11), 2341–2354. [https://doi.org/10.1175/1520-0485\(2003\)033<2341:rsftac>2.0.co;2](https://doi.org/10.1175/1520-0485(2003)033<2341:rsftac>2.0.co;2)
- Marshall, J., & Radko, T. (2006). A model of the upper branch of the meridional overturning of the Southern Ocean. *Progress in Oceanography*, 70(2–4), 331–345. <https://doi.org/10.1016/j.pocean.2006.07.004>
- Marshall, J., Scott, J. R., Romanou, A., Kelley, M., & Leboissetier, A. (2017). The dependence of the oceans MOC on mesoscale eddy diffusivities: A model study. *Ocean Modelling*, 111, 1–8. <https://doi.org/10.1016/j.ocemod.2017.01.001>
- Marshall, J., Shuckburgh, E., Jones, H., & Hill, C. (2006). Estimates and implications of surface eddy diffusivity in the Southern Ocean derived from tracer transport. *Journal of Physical Oceanography*, 36(9), 1806–1821. <https://doi.org/10.1175/jpo2949.1>
- Mason, E., Pascual, A., & McWilliams, J. C. (2014). A new sea surface height–based code for oceanic mesoscale eddy tracking. *Journal of Atmospheric and Oceanic Technology*, 31(5), 1181–1188. <https://doi.org/10.1175/jtech-d-14-00019.1>
- McGillicuddy, D., Jr., Anderson, L., Doney, S., & Maltrud, M. (2003). Eddy-driven sources and sinks of nutrients in the upper ocean: Results from a 0.1° resolution model of the North Atlantic. *Global Biogeochemical Cycles*, 17(2). <https://doi.org/10.1029/2002gb001987>
- Moore, E. H. (1920). On the reciprocal of the general algebraic matrix. *Bulletin of the American Mathematical Society*, 26, 394–395.
- Naveira Garabato, A. C., Ferrari, R., & Polzin, K. L. (2011). Eddy stirring in the Southern Ocean. *Journal of Geophysical Research*, 116(C9), C09019. <https://doi.org/10.1029/2010jc006818>
- Penrose, R. (1955). A generalized inverse for matrices. *Mathematical Proceedings of the Cambridge Philosophical Society*, 51(3), 406–413. <https://doi.org/10.1017/s0305004100030401>
- Prandtl, L. (1925). Bericht über Untersuchungen zur ausgebildeten Turbulenz. *ZAMM-Journal of Applied Mathematics and Mechanics/Zeitschrift für Angewandte Mathematik und Mechanik*, 5(2), 136–139. <https://doi.org/10.1002/zamm.19250050212>
- Redi, M. H. (1982). Oceanic isopycnal mixing by coordinate rotation. *Journal of Physical Oceanography*, 12(10), 1154–1158. [https://doi.org/10.1175/1520-0485\(1982\)012<1154:oimbc>2.0.co;2](https://doi.org/10.1175/1520-0485(1982)012<1154:oimbc>2.0.co;2)
- Rhines, P. (1970). Edge-bottom-and Rossby waves in a rotating stratified fluid. *Geophysical & Astrophysical Fluid Dynamics*, 1(3–4), 273–302. <https://doi.org/10.1080/03091927009365776>
- Riha, S., & Eden, C. (2011). Lagrangian and Eulerian lateral diffusivities in zonal jets. *Ocean Modelling*, 39(1–2), 114–124. <https://doi.org/10.1016/j.ocemod.2011.02.002>
- Roach, C. J., Balwada, D., & Speer, K. (2018). Global observations of horizontal mixing from Argo float and surface drifter trajectories. *Journal of Geophysical Research: Oceans*, 123(7), 4560–4575. <https://doi.org/10.1029/2018jc013750>
- Rypina, I. I., Kamenkovich, I., Berloff, P., & Pratt, L. J. (2012). Eddy-induced particle dispersion in the near-surface North Atlantic. *Journal of Physical Oceanography*, 42(12), 2206–2228. <https://doi.org/10.1175/jpo-d-11-0191.1>
- Siegenthaler, U. (1983). Uptake of excess CO<sub>2</sub> by an outcrop-diffusion model of the ocean. *Journal of Geophysical Research*, 88(C6), 3599–3608. <https://doi.org/10.1029/jc088ic06p03599>
- Smith, K. S. (2005). Tracer transport along and across coherent jets in two-dimensional turbulent flow. *Journal of Fluid Mechanics*, 544(-1), 133–142. <https://doi.org/10.1017/s0022112005006750>

- Smith, K. S. (2007a). Eddy amplitudes in baroclinic turbulence driven by nonzonal mean flow: Shear dispersion of potential vorticity. *Journal of Physical Oceanography*, 37(4), 1037–1050. <https://doi.org/10.1175/jpo3030.1>
- Smith, K. S. (2007b). The geography of linear baroclinic instability in Earth's oceans. *Journal of Marine Research*, 65(5), 655–683. <https://doi.org/10.1357/002224007783649484>
- Smith, K. S., & Marshall, J. (2009). Evidence for enhanced eddy mixing at middepth in the Southern Ocean. *Journal of Physical Oceanography*, 39(1), 50–69. <https://doi.org/10.1175/2008jpo3880.1>
- Smith, K. S., & Vanneste, J. (2013). A surface-aware projection basis for quasigeostrophic flow. *Journal of Physical Oceanography*, 43(3), 548–562. <https://doi.org/10.1175/jpo-d-12-0107.1>
- Smith, R. D., & Gent, P. R. (2004). Anisotropic Gent–McWilliams parameterization for ocean models. *Journal of Physical Oceanography*, 34(11), 2541–2564. <https://doi.org/10.1175/jpo2613.1>
- Stammer, D. (1998). On eddy characteristics, eddy transports, and mean flow properties. *Journal of Physical Oceanography*, 28(4), 727–739. [https://doi.org/10.1175/1520-0485\(1998\)028<0727:oeeceta>2.0.co;2](https://doi.org/10.1175/1520-0485(1998)028<0727:oeeceta>2.0.co;2)
- Stanley, Z., Bachman, S., & Grooms, I. (2020). Vertical structure of ocean mesoscale eddies with implications for parameterizations of tracer transport. *Journal of Advances in Modeling Earth Systems*, 12(10), e2020MS002151. <https://doi.org/10.1029/2020ms002151>
- Steinberg, J. M., Pelland, N. A., & Eriksen, C. C. (2019). Observed evolution of a California Undercurrent eddy. *Journal of Physical Oceanography*, 49(3), 649–674. <https://doi.org/10.1175/jpo-d-18-0033.1>
- Sun, L., Haigh, M., Shevchenko, I., Berloff, P., & Kamenkovich, I. (2021). On non-uniqueness of the mesoscale eddy diffusivity. *Journal of Fluid Mechanics*, 920. <https://doi.org/10.1017/jfm.2021.472>
- Tailleux, R., & McWilliams, J. C. (2001). The effect of bottom pressure decoupling on the speed of extratropical, baroclinic Rossby waves. *Journal of Physical Oceanography*, 31(6), 1461–1476. [https://doi.org/10.1175/1520-0485\(2001\)031<1461:teobpd>2.0.co;2](https://doi.org/10.1175/1520-0485(2001)031<1461:teobpd>2.0.co;2)
- Taylor, G. I. (1922). Diffusion by continuous movements. *Proceedings of the London Mathematical Society*, 2(1), 196–212. <https://doi.org/10.1112/plms/s2-20.1.196>
- Taylor, G. I. (1953). Dispersion of soluble matter in solvent flowing slowly through a tube. *Proceedings of the Royal Society of London A*, 219(1137), 186–203.
- Thompson, A. F. (2010). Jet formation and evolution in baroclinic turbulence with simple topography. *Journal of Physical Oceanography*, 40(2), 257–278. <https://doi.org/10.1175/2009jpo4218.1>
- Thompson, A. F., & Young, W. R. (2006). Scaling baroclinic eddy fluxes: Vortices and energy balance. *Journal of Physical Oceanography*, 36(4), 720–738. <https://doi.org/10.1175/jpo2874.1>
- Tulloch, R., Ferrari, R., Jahn, O., Klocker, A., LaCasce, J., Ledwell, J. R., et al. (2014). Direct estimate of lateral eddy diffusivity upstream of drake passage. *Journal of Physical Oceanography*, 44(10), 2593–2616. <https://doi.org/10.1175/jpo-d-13-0120.1>
- Tulloch, R., Marshall, J., Hill, C., & Smith, K. S. (2011). Scales, growth rates, and spectral fluxes of baroclinic instability in the ocean. *Journal of Physical Oceanography*, 41(6), 1057–1076. <https://doi.org/10.1175/2011jpo4404.1>
- Visbeck, M., Marshall, J., Haine, T., & Spall, M. (1997). Specification of eddy transfer coefficients in coarse-resolution ocean circulation models. *Journal of Physical Oceanography*, 27(3), 381–402. [https://doi.org/10.1175/1520-0485\(1997\)027<0381:soetci>2.0.co;2](https://doi.org/10.1175/1520-0485(1997)027<0381:soetci>2.0.co;2)
- Waterman, S., & Jayne, S. R. (2011). Eddy-mean flow interactions in the along-stream development of a western boundary current jet: An idealized model study. *Journal of Physical Oceanography*, 41(4), 682–707. <https://doi.org/10.1175/2010jpo4477.1>
- Wei, H., & Wang, Y. (2021). Full-depth scalings for isopycnal eddy mixing across continental slopes under upwelling-favorable winds. *Journal of Advances in Modeling Earth Systems*, 13(6), e2021MS002498. <https://doi.org/10.1029/2021ms002498>
- Wolfe, C. L. (2014). Approximations to the ocean's residual circulation in arbitrary tracer coordinates. *Ocean Modelling*, 75, 20–35. <https://doi.org/10.1016/j.ocemod.2013.12.004>
- Wolfe, C. L., & Cessi, P. (2009). Overturning circulation in an eddy-resolving model: The effect of the pole-to-pole temperature gradient. *Journal of Physical Oceanography*, 39(1), 125–142. <https://doi.org/10.1175/2008jpo3991.1>
- Wolfe, C. L., & Cessi, P. (2010). What sets the strength of the middepth stratification and overturning circulation in eddying ocean models? *Journal of Physical Oceanography*, 40(7), 1520–1538. <https://doi.org/10.1175/2010jpo4393.1>
- Wolfe, C. L., & Cessi, P. (2011). The adiabatic pole-to-pole overturning circulation. *Journal of Physical Oceanography*, 41(9), 1795–1810. <https://doi.org/10.1175/2011JPO4570.1>
- Wolfe, C. L., Cessi, P., McClean, J. L., & Maltrud, M. E. (2008). Vertical heat flux in eddying ocean models. *Geophysical Research Letters*, 35(23), L23605. <https://doi.org/10.1029/2008GL036138>
- Wolfram, P. J., & Ringler, T. D. (2017). Quantifying residual, eddy, and mean flow effects on mixing in an idealized circumpolar current. *Journal of Physical Oceanography*, 47(8), 1897–1920. <https://doi.org/10.1175/jpo-d-16-0101.1>
- Wolfram, P. J., Ringler, T. D., Maltrud, M. E., Jacobsen, D. W., & Petersen, M. R. (2015). Diagnosing isopycnal diffusivity in an eddying, idealized midlatitude ocean basin via Lagrangian, in Situ, Global, High-Performance Particle Tracking (LIGHT). *Journal of Physical Oceanography*, 45(8), 2114–2133. <https://doi.org/10.1175/jpo-d-14-0260.1>
- Wunsch, C. (1997). The vertical partition of oceanic horizontal kinetic energy. *Journal of Physical Oceanography*, 27(8), 1770–1794. [https://doi.org/10.1175/1520-0485\(1997\)027<1770:tvpooh>2.0.co;2](https://doi.org/10.1175/1520-0485(1997)027<1770:tvpooh>2.0.co;2)
- Young, W., Rhines, P., & Garrett, C. (1982). Shear-flow dispersion, internal waves and horizontal mixing in the ocean. *Journal of Physical Oceanography*, 12(6), 515–527. [https://doi.org/10.1175/1520-0485\(1982\)012<0515:sfdiwa>2.0.co;2](https://doi.org/10.1175/1520-0485(1982)012<0515:sfdiwa>2.0.co;2)
- Zhang, Z., Wang, W., & Qiu, B. (2014). Oceanic mass transport by mesoscale eddies. *Science*, 345(6194), 322–324. <https://doi.org/10.1126/science.1252418>
- Zhurbas, V., Lyzhkov, D., & Kuzmina, N. (2014). Drifter-derived estimates of lateral eddy diffusivity in the world ocean with emphasis on the Indian Ocean and problems of parameterisation. *Deep-Sea Research I*, 83, 1–11. <https://doi.org/10.1016/j.dsr.2013.09.001>
- Zhurbas, V., & Oh, I. S. (2003). Lateral diffusivity and Lagrangian scales in the Pacific Ocean as derived from drifter data. *Journal of Geophysical Research*, 108(C5), 3141. <https://doi.org/10.1029/2002jc001596>
- Zhurbas, V., & Oh, I. S. (2004). Drifter-derived maps of lateral diffusivity in the Pacific and Atlantic oceans in relation to surface circulation patterns. *Journal of Geophysical Research*, 109(C5), C05015. <https://doi.org/10.1029/2003jc002241>